공학박사 학위논문

Methane dehydroaromatization over Mo/H-MCM-22 and Mn/H-ZSM-5 catalyst

Mo/H-MCM-22 및 Mn/H-ZSM-5 촉매 상에서 메탄탈수소방향족화 반응

2019 년 2 월

서울대학교 대학원

화학생물공학부

임 태 환

Abstract

Methane dehydroaromatization over Mo/H-MCM-22 and Mn/H-ZSM-5 catalyst

Tae Hwan Lim
School of Chemical and Biological Engineering
The Graduate School
Seoul National University

Natural gas is as clean energy resource, which is abundantly distributed all over the world so that it has been drawn much attention as an alternative energy resource to produce valuable chemicals instead of crude oil. However, some natural gas have been flared or vented, which accounts for approximately 5% of world annual natural gas consumption. Main component of natural gas is methane, which is potent greenhouse gas whose global warming potential is 21times higher than that of carbon dioxide. Thus, the effective use of methane is necessary to reduce emission of greenhouse gas.

Methane can be converted to higher hydrocarbon via direct or indirect method. Between both methods, study on the methane conversion has been mostly applied to indirect method. However, the disadvantage of indirect method lies in the fact that it needs higher cost and longer time for operation than direct method since the indirect

method consists of a two-step process. Accordingly, many studies for the direct method having an economical advantage have been conducted to convert methane into higher hydrocarbon for decades. Among the various direct methods, methane dehydroaromatization (MDA) reaction has attracted considerable attention because it is more thermodynamically favorable in converting methane into benzene than other products. Although the MDA reaction has been studied for over 20 years, studies on the catalyst containing new metal and support are still necessary to improve catalytic activity and suppress the deactivation of catalyst for commercialization of MDA process.

In order to investigate the effect of zeolite controlling Si/Al_2 ratio on the performance and deactivation of catalyst for MDA reaction, Mo(5)/H-MCM-22 catalysts with various Si/Al_2 ratios were applied to MDA reaction. According to the NH_3 TPD, XPS, TPO, UV Raman and STEM-EDS analysis, it is clearly demonstrated that Brønsted acid site, determined by the Si/Al_2 ratios, stabilizes monomeric Mo oxide species, by facilitating to migrate Mo oxides into the microchannel of zeolite, so that it can influence the distribution of catalytically active Mo oxide species. Combined TPO and UV Raman analysis of post-reaction catalysts obviously confirmed that HT (high temperature) type coke is mainly composed of polyaromatics such as naphthalene and anthracene, which brings about the deactivation of the catalyst during MDA reaction. The formation of HT type coke is mainly affected by the amount of Mo oxides present on the external surface of zeolite, which exhibits that the major role of zeolite microchannel is to provide a shape-selective environment during the conversion of methane to benzene. To sum up, an increment in Brønsted acid site enhances the dispersion of Mo oxides, thus leading

to the improved methane conversion rate and benzene formation rate while suppressing the formation of HT type coke concomitantly.

To examine the effect of various manganese species on the performance and deactivation of catalyst for MDA reaction, Mn/H-ZSM-5 catalysts with various loading amounts of Mn were applied to the MDA reaction. Combined H_2 TPR, NH_3 TPD, and DRIFT analysis indicates that the presence of various manganese species, such as isolated Mn^{2+} ion, isolated Mn^{3+} ion, agglomerated MnO, and agglomerated Mn_2O_3 species, depends on the loading amount of Mn. Among these species, it is demonstrated that at Mn loading below 5wt%, isolated Mn^{2+} ion and isolated Mn^{3+} ion species are primarily produced by a linkage of Mn^{2+} ion to Brønsted acid site and hydroxyl groups (ex-Al-OH and Si-OH) in zeolite, respectively. By contrast, at Mn loading above 5wt%, agglomerated MnO and Mn_2O_3 species become abundant on the external surface of zeolite without anchoring to any sites, as evidenced by H_2 TPR and XPS analysis. Among the manganese species, isolated Mn^{3+} ion species plays an essential role as a precursor of active site for the MDA reaction. On the other hand, agglomerated MnO and Mn_2O_3 species diminish catalytic activity by blocking the entrance of the micro channel of zeolite. Combined H_2 TPR, TPO, and UV Raman analysis proves that the isolated Mn^{2+} ion species is produced from the reduction of isolated Mn^{3+} ion species by CH_4 and subsequent conversion into new manganese species that cannot be oxidized again. As the reaction proceeds, carbonaceous deposit species is excessively formed on the active manganese species, which results in the deactivation of the catalyst due to the blocked access of methane to active sites. In summary, the new manganese species produced from the isolated Mn^{3+} ion species during the initial stage of MDA reaction serves as a main active

site, while the formation of excessive carbonaceous deposit species on the active manganese species is a primary reason for the deactivation of catalyst.

Keywords: Methane dehydroaromatization; Mo/H-MCM-22; Deactivation of catalyst; Si/Al_2 ratio; Brønsted acid site; Mn/H-ZSM-5; Manganese species

Student Number: 2015-30217

Contents

List of Tables

List of Figures

Chapter 1. Introduction

To date, crude oil has produced a large amount of energy as the main resource of energy production. In addition, many valuable chemicals have been produced mostly from crude oil. However, new energy resource is needed for synthesis of valuable chemicals due to the depletion of crude oil resource in recent decades.

As exhibited in Figure 1-1, natural gas is as clean energy resource, which is plentifully distributed all over the world [1, 2]. The proven reserves of natural gas have increased considerably from the last two decades as presented in Figure 1-2, and it is suggested that estimates will keep on for more than two centuries [1]. Thus, it has been attracted considerable attention as an alternative energy resource to manufacture valuable products.

Currently, natural gas has been used in various fields (such as electric power, industrial, residential, commercial and transportation) [3]. However, it has been estimated that about 150 billion m^3 of natural gas, which accounts for approximately 5% of world annual natural gas consumption, has been flared or vented yearly all over the world [4]. Main component of natural gas is methane, and emitted methane is potent greenhouse gas where its global warming potential is 21times higher than that of carbon dioxide and therefore it can accelerate the global warming [5, 6]. Hence, the effective use of methane is necessary to reduce emission of greenhouse gas.

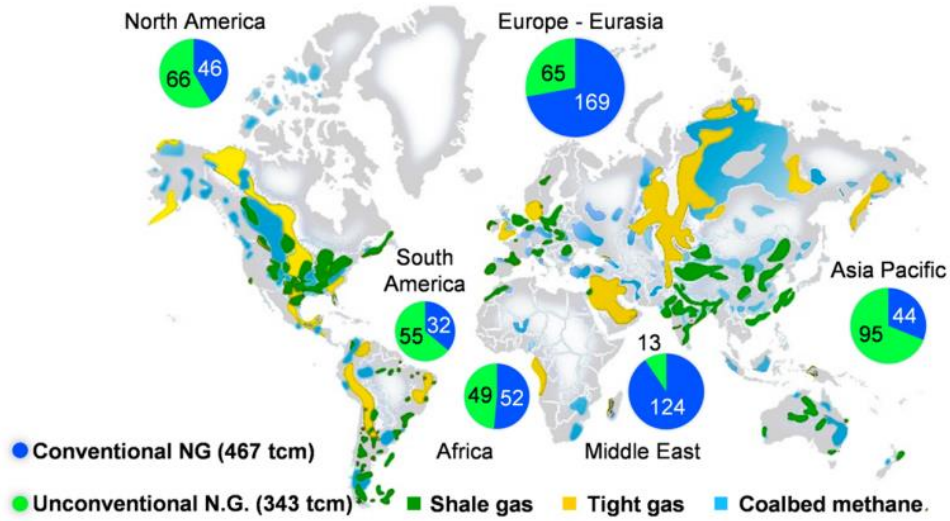

Figure 1-1. World map for conventional and unconventional natural gas potential [1].

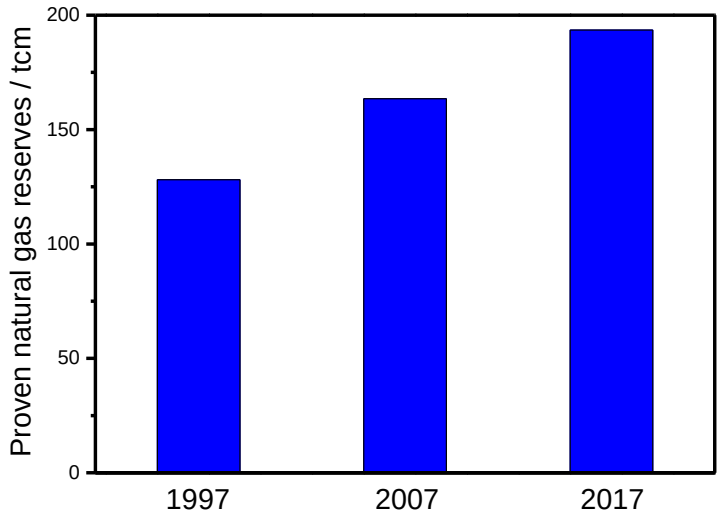

Figure 1-2. Proven natural gas reserves in trillion cubic meter. (Data taken from BP Statistical Review of World Energy [7])

1.1. Methane dehydroaromatization

To date, it has been receiving considerable attention to convert methane into more valuable hydrocarbon products. Methane can be converted to higher hydrocarbon via direct or indirect methods, as indicated in Figure 1-3 [8]. The indirect method is constituted of two steps. The first step is to convert methane into synthesis gas through steam reforming, CO_2 reforming or partial oxidation and then the second step is to produce high value products from the synthesis gas via a Fischer-Tropsch process. The disadvantage of indirect method lies in the fact that it needs longer time and higher cost for operation than direct method. By contrast, the direct method is to convert methane into higher hydrocarbon at one-step, which has an economical advantage due to the absence of the intermediate step to produce the synthesis gas [9].

Between direct methods performed under oxidative and nonoxidative condition, nonoxidative conversion of methane is considered as more promising since it has higher selectivity of desired products than the counterpart does. Particularly, methane dehydroaromatization (MDA) reaction has attracted much attention because it is more thermodynamically favorable in converting methane into benzene than other products, in spite of the thermodynamically high energy requirements [10].

$$6CH_4(g) \rightarrow C_6H_6(g) + 9H_2(g)$$

$$\Delta rG^{o}_{298} = +\ 433\ kJ/mol,\ \Delta rH^{o}_{298} = +\ 531\ kJ/mol \qquad (1)$$

Wang et al. firstly reported that the MDA reaction in 1993 exhibits the production of benzene and hydrogen from methane under atmospheric pressure over Mo/HZSM-5 catalyst at 700 ℃ [11]. They suggested Mo/HZSM-5 catalyst, which shows excellent methane conversion and selectivity of benzene for MDA reaction. Accordingly, the performance of MDA reaction over active metal (such as Mo, W, Zn, Re, Mn and Cr) impregnated ZSM-5 zeolite has been much studied [12-16]. Among these active metals, however, Mo metal has the best catalytic activity for MDA reaction until now.

On the other hand, Ma et al. reported that medium pore zeolites such as ZSM-5 and MCM-22 can have a positive effect on the formation of benzene since they possess both two-dimensional pore structure and pore diameter close to kinetic diameter of benzene molecule (about 6.0 Å) [8]. It underlines that pore structure and size of the zeolite influence on the kinds of product formed during the MDA reaction.

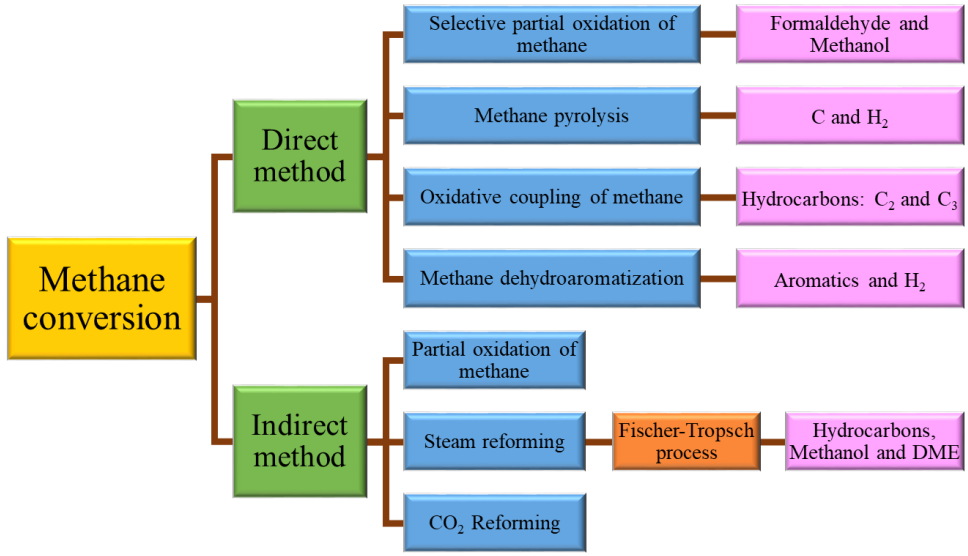

Figure 1-3. Two routes for methane conversion.

1.2. Objectives

Natural gas is regarded as an alternative energy resource to produce valuable chemicals instead of crude oil. However, since flared or vented methane from natural gas reserves is potent greenhouse gas, the remaining methane must be used effectively to reduce emission of greenhouse gas. Among the various methods for methane conversion, MDA reaction has attracted much attention because it is more thermodynamically favorable in converting methane into benzene than other products. Although the MDA reaction has been studied for over 20 years, studies about catalyst containing new metal and support are still important to enhance catalytic activity and suppress the deactivation of catalyst for commercialization of MDA process.

In this respect, this thesis mainly consists of investigating zeolite as a support and active metal to find out their active site and deactivation mechanism for the MDA reaction. In Chapter 2, Mo impregnated H-MCM-22 zeolites with various the Si/Al_2 ratios were evaluated in order to examine the migration of Mo oxide species into the micropore of zeolite, which is regarded as active site, and the formation of carbonaceous deposit. Furthermore, the effect of such characteristics on MDA reaction was investigated. In Chapter 3, Mn impregnated H-ZSM-5 zeolites with changing the loading amount of Mn were assessed to investigate the effect of various manganese species on the MDA reaction. In addition, the activation and deactivation mechanism of Mn based catalyst were examined by comparing the characteristics of the catalysts as the reaction proceeds.

Chapter 2. Effect of Si/Al_2 ratios in Mo/H-MCM-22 on methane dehydroaromatization

2.1. Introduction

Methane, a main component of natural gas and shale gas, is the most abundant hydrocarbon resource and has drawn much attention as an alternative energy by converting methane to more valuable hydrocarbon products through indirect and direct methods. The indirect method consists of two steps. The first step is to convert methane into synthesis gas through steam reforming, dry reforming or partial oxidation and the second step is to produce high value products from the synthesis gas via a Fischer-Tropsch process. By contrast, the direct method is to convert methane into higher hydrocarbon at one-step, which has an economical advantage due to the absence of the intermediate step to produce the synthesis gas [2, 9]. Between two kinds of direct method performed under oxidative and nonoxidative condition, nonoxidative conversion of methane is considered as more promising since it has higher selectivity of desired products than the counterpart does. In particular, MDA reaction has been receiving considerable attention because it is more thermodynamically favorable in converting methane into benzene than other products [10].

Wang et al. firstly reported the MDA reaction in 1993, which exhibits the production of benzene and hydrogen from methane under atmospheric pressure over Mo/HZSM-5 catalyst at 700 ℃ [11]. The performances of MDA reaction over molybdenum impregnated ZSM-5 or MCM-22 have been mostly studied until now

[17-19]. Ma et al. proposed that medium pore zeolites such as ZSM-5 and MCM-22 can have a positive effect on MDA reaction because they possess both two-dimensional pore structures and pore diameters close to kinetic diameter of benzene molecule (about 6.0 Å) [8]. Specifically, MCM-22 has two independent multidimensional pore systems unlike ZSM-5. One is 2 dimensional (2D) 10-membered ring sinusoidal channel system (4.0 × 5.0 Å) and the other is 3 dimensional (3D) 12-membered ring supercage system (7.1 Å × 7.1 Å × 18.4 Å) interconnected by 10-membered ring windows (4.0 × 5.5 Å) [20]. Compared to ZSM-5, such unique structure and smaller pore size of MCM-22 than that of ZSM-5 are expected to provide a high accommodation ability of carbonaceous deposit and high benzene formation rate under shape-selective environment during MDA reaction [21, 22].

Several reaction mechanisms for MDA reaction have been suggested by many research groups [18, 23-26]. Among these reaction mechanisms, bifunctional mechanism has been commonly accepted in MDA reaction. It employs Mo_2C (or MoO_xC_y) and the Brønsted acid site (BAS) of the zeolite as two active sites, and the mechanism proceeds as follows: dehydrogenation and coupling of methane at Mo_2C (or MoO_xC_y) produce ethylene, and then the ethylene is oligomerized to benzene on the BAS in the micropore of zeolite [26, 27]. By contrast, some groups proposed monofunctional mechanism for MDA reaction [23, 25]. They insisted that both the conversion of methane to C_2 intermediates (C_2H_y, $y < 4$) and the aromatization of the C_2 intermediates exclusively occur over Mo_2C located inside the micropore of zeolite.

One important factor for MDA reaction lies in the migration of Mo oxide species into the micropore of zeolite as suggested by many previous reports [19, 28-30]. They insisted that Mo oxides present on the external surface diffuse and migrate into the micropores during the calcination above their Tamman temperature. Then, Mo oxides species anchor to BAS in micropores, originating from an exchanging with the acidic H atom. During the initial period of MDA reaction, Mo oxides species are carburized to Mo carbide species like Mo_2C (or MoO_xC_y) which are known as an active site of methane activation. Thus, migration of Mo oxides species into microchannel enhances the activity for MDA reaction [29]. Furthermore, several groups proposed that catalytic performance for MDA reaction is related to the anchoring mode of molybdenum inside the micropore of zeolite [31, 32].

Another important factor for MDA reaction is carbonaceous deposits which are major unwanted byproducts produced during MDA reaction since it causes rapid deactivation of the Mo containing zeolite catalyst [17, 33-35]. In particular, carbonaceous deposit derived from polyaromatic hydrocarbon has widely accepted as the main reason for the deactivation of catalyst among various carbonaceous deposits, and, in addition, it can be formed on the BAS located at the external surface of the zeolite [34, 36]. To date, there have been many studies about the modification of BAS in zeolite, which affects the production of carbonaceous deposit via the appropriate post-synthesis modifications such as silylation and dealumination under thermal and hydrothermal condition [37-40]. However, to the best of our knowledge, there is no previous research about the reactivity and the formation of carbonaceous deposits for MDA reaction in Mo/H-MCM-22 catalysts as a function of Si/Al_2 ratio.

In addition, although there was a previous study that applied Mo/H-MCM-22 catalysts with various Si/Al_2 ratio to MDA reaction, it did not examine in detail about the role of BAS in MDA activity [41].

In this study, we aimed to examine the migration of Mo oxide species into the micropore of zeolite and the formation of carbonaceous deposit in detail while varying the Si/Al_2 ratios of MCM-22 zeolite. Furthermore, we attempted to investigate the effect of such characteristics on MDA reaction.

2.2. Experimental

2.2.1. Catalysts preparation

MCM-22 was synthesized with various Si/Al_2 ratios of 21, 45 and 91 via hydrothermal synthesis method suggested by Corma et al. [42]. Synthesis mixtures were prepared by using hexamethyleneimine (HMI, 99%, Sigma Aldrich), Sodium aluminate (50%-56% Al_2O_3, 40-45% Na_2O, Sigma Aldrich), Fumed SiO_2 (Sigma Aldrich), NaOH (≥ 98%, Sigma Aldrich) and deionized water through the synthesis parameters, as indicated in Table 2-1. The hydrothermal synthesis was carried out in a Teflon-lined autoclave while rotating (60 rpm) at 150 ℃ for selected times. The MCM-22 catalyst with various Si/Al_2 ratios was denoted as MCM-22 (X), where X is an actual Si/Al_2 ratio of MCM-22 obtained from ICP-AES results, as presented in Table 2-1. The hydrogen forms of the MCM-22 catalysts were obtained after ion exchange twice with 1 M NH_4NO_3 aqueous solution while stirring at 80 ℃ for 6 h followed by calcination in a muffle furnace at 500 °C for 8 h.

5wt% of Mo was impregnated on the H-MCM-22 zeolites with various Si/Al_2 ratios by using an aqueous solution of ammonium heptamolybdate, which are denoted as Mo(5)/H-MCM-22 (X) catalysts. The resulting samples were dried at 105 ℃ overnight and then calcined in a muffle furnace at 500 °C for 4 h. After the calcination, the catalysts were crushed and sieved to 20-40 mesh granules for catalytic experiments.

Table 2-1. Synthesis parameters and Si/Al_2 ratio obtained from ICP-AES analysis for MCM-22 zeolites with various Si/Al_2 ratios.

Catalyst	Gel composition					Time (days)	Si/Al_2 ratio (ICP AES)
	SiO_2/Al_2O_3	OH/SiO_2	Na/SiO_2	HMI/SiO_2	H_2O/SiO_2		
MCM-22 (21)	30	0.30	0.30	0.50	40	7	21
MCM-22 (45)	50	0.14	0.14	0.35	45	7	45
MCM-22 (91)	100	0.12	0.18	0.35	35	8	91

2.2.2. Catalysts characterization

Inductively coupled plasma-atomic emission spectroscopy (ICP-AES), ICPE-9000 (Shimadzu), was applied to obtain actual atomic Si/Al_2 ratios for MCM-22 samples.

The morphology of MCM-22 samples was investigated by using field emission scanning electron microscopy (FE-SEM), MERLIN Compact (ZEISS) after coated with platinum film.

The crystal structure of the catalysts was verified by using the powder X-ray diffraction (XRD). XRD analysis was performed on a SmartLab (Rigaku) with Cu Kα radiation at 30 mA and 40 kV. The XRD patterns were collected in a 2θ range from 5 ° to 40 ° with the scanning step size of 0.02 ° at a speed of 2 °/min.

Textural properties of the samples were measured by N_2 physisorption at -195.7 ℃ in ASAP 2010 (Micromeritics) using the Brunauer-Emmett-Teller (BET) and t-plot method. Prior to the measurement, all samples were degassed under evacuated condition at 300 ℃ for at least 10 h.

Temperature programed desorption of NH_3 (NH_3 TPD) was carried out to estimate the amount of acid sites in Mo containing zeolites with a thermal conductivity detector (TCD) in a BEL-CAT BASIC (BEL Japan Inc.). At first, 0.05 g of samples loaded on quartz wool in a U-shaped quartz tube was pre-treated under He flow at 400 ℃ for 1 h and then cooled down to 120 ℃. Then, the sample was exposed to 5% NH_3/He gas at 120 ℃ for 1 h, and subsequently purged under He flow at 120 ℃ for 1 h to eliminate weakly adsorbed NH_3 molecules from the surface. After that, they were heated to 900 ℃ with He flow at a heating rate of 10 °C/min.

X-ray photoelectron spectroscopy (XPS) analysis of the catalysts was performed with a K-alpha (Thermo Scientific Inc., U.K.) in order to investigate the relative surface concentration of Mo element in catalysts. The instrument uses a 400 μm-diameter beam and a focused monochromatic Al Kα X-ray (1486.6 eV) source operated at 36 W.

UV Raman analysis of the fresh and post-reaction samples was conducted to identify Mo oxides species and carbonaceous deposit species present on the zeolite surface, respectively. UV Raman spectra were recorded with a Renishaw (In Via Raman Microscope), equipped with CCD detector. The 244 nm line of an Ar laser was used as the excitation source.

Scanning transmission electron microscopy (STEM) and Energy dispersive spectroscopy (EDS) analysis was carried out at an accelerating voltage of 200 kV in a JEM-ARM200F (JEOL Ltd) electron microscope equipped with Spherical aberration corrector and Field emission gun. The suspension was prepared by dispersing small amount of samples in ethanol. Drops of the suspension were deposited on a carbon-coated Cu grid and dried at 60 ℃. Low dwell time and averaging over several accumulations were used to minimize beam damage of the samples and beam tracking was applied to avoid drift during the EDS mapping analysis.

Temperature programed oxidation (TPO) was performed to investigate the nature of carbonaceous deposits by using a BEL-CAT-II (MicrotracBEL, Corp.) with a TCD. Without pretreatment, about 0.05 g of post-reaction samples was heated from 30 ℃ to 800 ℃ with 5% O_2/He at a heating rate of 5 °C/min. The main products are

CO and CO_2 since H_2O trap was used to remove H_2O produced during the oxidation. Here, it is reported that detection curves for CO and CO_2 species have similar shape each other [33]. Thus, we employed CO_x (the amount of CO added to that of CO_2) as an only produced species in this analysis.

2.2.3. Catalytic activity measurement

The MDA reaction was carried out over 0.2 g of the catalyst having 20-40 mesh size under atmospheric pressure in a fixed-bed quartz reactor. The catalyst was heated to 680 ℃ and maintained for 0.5 h in a He flow rate of 20 ml/min. Then, 10% N_2/CH_4 gas mixture was fed to the reactor at a flow rate of 10 ml/min. Schematic view of MDA reaction system is presented in Figure 2-1. The effluent gases were analyzed at regular intervals by an on-line gas chromatograph (YL6500GC) equipped with two columns (GS-Gaspro and Carboxen-1000 column) and two detectors (flame ionization detector and thermal conductivity detector). The outlet pipe line from the end of a quartz reactor to GC column, containing on-line sampling valve, were maintained at 230 ℃ to avoid the condensation and strong adsorption of the hydrocarbon products. By using a nitrogen gas as an internal standard, the methane conversion, selectivity of the product and carbonaceous deposits, were evaluated on the basis of carbon mass balance, as suggested by Liu et al. [43]. The methane conversion, selectivity of the product ($S_{Product}^{Carbon}$) were calculated from Eq. (2) and (3). The selectivity of carbonaceous deposits ($S_{deposits}^{Carbonaceous}$) containing amorphous carbon, graphitic carbon and undetected heavy aromatic compounds was

calculated from Eq. (4). Here, *X*, *F* and N^{carbon} represent mole fraction, total gas flow rate and carbon number in a molecule, respectively.

$$F^{inlet}X_{N_2}^{inlet} = F^{outlet}X_{N_2}^{outlet} \tag{1}$$

$$\text{Conversion}(CH_4) = \frac{F^{inlet}X_{CH_4}^{inlet} - F^{outlet}X_{CH_4}^{outlet}}{F^{inlet}X_{CH_4}^{inlet}} = 1 - \frac{X_{CH_4}^{outlet}X_{N_2}^{inlet}}{X_{CH_4}^{inlet}X_{N_2}^{outlet}} \tag{2}$$

$$S_{Product}^{Carbon} = \frac{F^{outlet}X_{product}^{outlet}N_{Product}^{Carbon}}{F^{inlet}X_{CH_4}^{inlet} - F^{outlet}X_{CH_4}^{outlet}} = \frac{X_{N_2}^{inlet}X_{product}^{outlet}N_{Product}^{Carbon}}{X_{N_2}^{outlet}X_{CH_4}^{inlet} - X_{N_2}^{inlet}X_{CH_4}^{outlet}} \tag{3}$$

$$S_{deposits}^{Carbonaceous} = 1 - \sum S_{Product}^{Carbon} \tag{4}$$

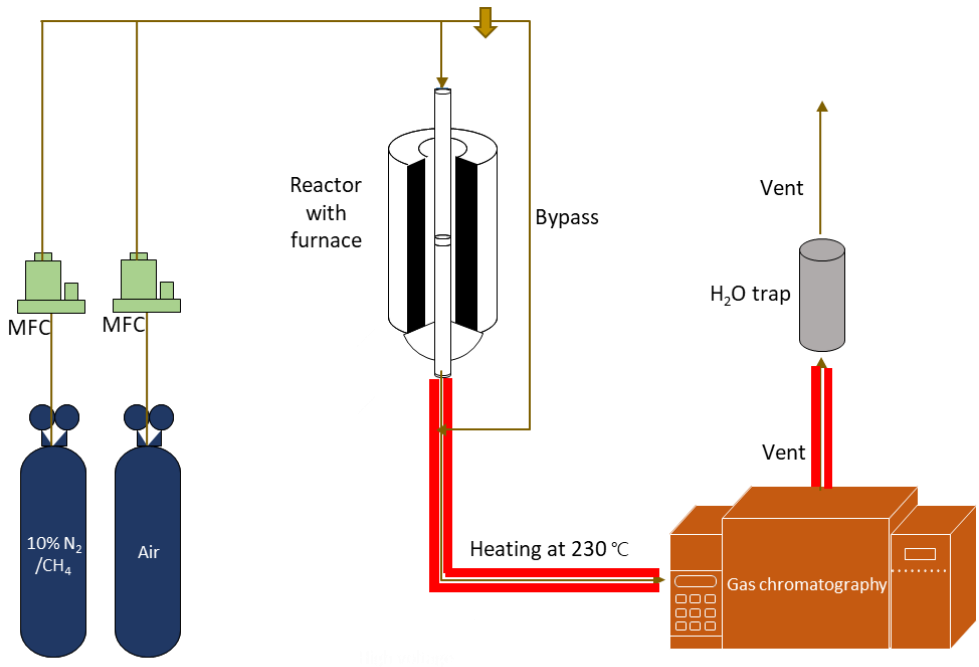

Figure 2-1. Schematic view of MDA reaction system.

2.3. Results

2.3.1. Characterization of fresh catalysts

XRD patterns for MCM-22 and Mo(5)/H-MCM-22 samples with Si/Al_2 ratios of 21, 45 and 91 are indicated in Figure 2-2. The XRD patterns for all the samples are almost matched with those of MCM-22 reported by Corma et al. [42]. In order to compare the extent of crystallization, relative crystallinity of the MCM-22 samples was estimated by using an intensity of the peak at 2θ of 26.1° [20]. As summarized in Table 2-2, the relative crystallinity for the MCM-22 samples with the Si/Al_2 ratios of 21, 45 and 91 are 100%, 96% and 109%, respectively. In other words, all the MCM-22 samples have similar relative crystallinity irrespective of the Si/Al_2 ratio. In case of Mo(5)/H-MCM-22 samples, their relative crystallinity are more reduced than the MCM-22 ones by about 24-35% while XRD patterns are well corresponding to their zeolite supports. It is notable to point out the absence of MoO_3 crystallite patterns in all Mo containing samples, which shows that MoO_3 is highly dispersed on MCM-22 zeolite.

SEM analysis obviously confirmed morphology of all MCM-22 zeolites in the form of very thin platelets as exhibited in Figure 2-3(a)-(c).

The BET surface area and micropore volume of MCM-22 and Mo(5)/H-MCM-22 samples are listed in Table 2-2. The BET surface area and the micropore volume of MCM-22 (21) are 570 m^2/g and 0.191 cm^3/g, respectively, which are well matched with previous results [20, 44]. In addition, those of MCM-22 (45) are 565 m^2/g and 0.190 cm^3/g and those of MCM-22 (91) are 406 m^2/g and 0.144 cm^3/g, respectively.

Mo(5)/H-MCM-22 samples have lower BET surface areas (16-26%) and micropore volumes (16-26%) than those of their zeolite supports. The BET surface area, micropore volume and relative crystallinity are reduced significantly after Mo loading. It can be explained by ion exchange of ammonium nitrate and incorporation of Mo on bare MCM-22. Thus, although the BET surface area and micropore volume do not have clear tendency depending on Si/Al_2 ratios of MCM-22, it is confirmed that change of BET surface area and micropore volume are related to that of the relative crystallinity.

NH_3 TPD profiles of all MCM-22 and Mo(5)/H-MCM-22 catalysts pretreated at 680 ℃ for 0.5 h under He flow are displayed in Figure 2-4. The peak position and the amount of desorbed ammonia for NH_3 TPD profiles are summarized in Table 2-3. All MCM-22 samples have two main peaks located at lower temperature (about 184 ℃) and higher temperature (about 360 ℃). The former peak is assigned to the desorption of physisorbed NH_3 species and NH_3 species located at non-exchangeable cationic sites, referred to as weak acid site (WAS) [22]. The latter peak originates from the desorption of NH_3 species adsorbed on exchangeable protonic sites, denoted as Brønsted acid site (BAS) [22]. Table 2-3 clearly indicates that the amount of BAS in the samples increases with decreasing Si/Al_2 ratio and the descending order is as follow: MCM-22 (21) > MCM-22 (45) > MCM-22 (91). In case of Mo containing samples, a new peak located at about 281 ℃ appears, which is designated as medium strength acid site (MAS) while the amount of BAS decreases [22].

XPS analysis was conducted on Mo containing catalysts after calcination at 680 ℃ for 0.5 h in flowing He. The surface atomic composition and Mo/(Si + Al) ratio of

the catalysts obtained from XPS analysis are presented in Table 2-4. The ratios of Mo/(Si + Al) decrease as Si/Al_2 ratio decreases and, in particular, Mo(5)/H-MCM-22 (21) has the lowest Mo/(Si + Al) ratio among the catalysts. The different ratios of Mo/(Si + Al) underline the relative amount of Mo atom present on the zeolite surface because XPS is a surface analysis technique. Consequently, it is confirmed that the migration of Mo atom from surface into microchannel of zeolite increases as the Si/Al_2 ratio decreases.

UV Raman analysis of the bulk MoO_3, Mo(5)/H-MCM-22 and H-MCM-22 catalysts, pretreated at 680 ℃ for 0.5 h under He flow, was performed. The advantage of using a 244 nm laser excitation lies in the fact that it can avoid fluorescence interference and improve the characteristic bands associated with the isolated tetrahedral molybdates species since the laser is close to an absorbance band of the one at 220 nm [45]. Figure 2-5 shows UV Raman spectra of bulk MoO_3, Mo(5)/H-MCM-22 and H-MCM-22 samples. The Raman spectrum of the bulk MoO_3 sample exhibits two sharp Raman bands at 994 and 821 cm^{-1} ascribed to the symmetric stretching vibration of the Mo=O bond and the asymmetric stretching vibration of Mo-O-Mo bond, respectively [37, 46]. The Raman spectra of the H-MCM-22 samples demonstrate four Raman bands at 354, 469, 523 and 812 cm^{-1} of which characteristic has not identified yet. Once Mo was impregnated on the H-MCM-22 zeolite, the Raman bands of H-MCM-22 almost disappear while new Raman bands arising from molybdenyl stretching vibrations appear, as shown in the Raman spectra of Mo(5)/H-MCM-22 samples. Such change in Raman bands is known to be affected by the amount of Mo oxide present on the surface of zeolite

and selective enhancement of Raman bands associated with Mo oxides tetrahedral species [45, 47].

In the case of Mo containing samples, the Raman spectra exhibit a sharp band at ~995 cm^{-1} corresponding to the symmetric stretching vibration of surface isolated $Mo(=O)_2$ dioxo species in isolated monomeric Mo oxide species and a broad band between 660 and 930 cm^{-1} attributed to the symmetric and asymmetric stretching vibration of surface Mo-O-Mo species in polymeric Mo oxide species [46, 48]. The Raman band intensity of monomeric and polymeric Mo oxide species is compared in the Mo(5)/H-MCM-22 catalysts in order to investigate how the distribution of Mo oxide species present on the surface varies depending on Si/Al_2 ratios because UV Raman spectroscopy is surface sensitive technique. As the Si/Al_2 ratio increases, the Raman band intensity of monomeric Mo oxide species decreases while that of polymeric Mo oxide species increases. In other words, monomeric Mo oxide species are present on the surface more abundantly than polymeric Mo oxide species as the Si/Al_2 ratio decreases. Hence, it can be claimed that Mo oxide species are highly dispersed while suppressing the aggregation of Mo oxides present on the surface of zeolite with decreasing Si/Al_2 ratio.

It is worth to note that the sharp Raman band shifts from 990 to 1000 cm^{-1} in the Mo containing samples as the Si/Al_2 ratio decreases. The shift of surface isolated $Mo(=O)_2$ dioxo species to the high wavenumber implies the shortening of the Mo=O and Mo-O bonds due to the formation of a highly distorted surface species [46, 48]. It is proposed that the catalysts having the Si/Al_2 ratios above 50 possess an isolated Mo dioxo species anchored on single Al atom framework sites while the catalyst

having a Si/Al_2 ratio of 30 possesses an isolated Mo dioxo species anchored on double Al atom framework sites [31, 32, 49]. Moreover, Gao et al. claimed that Mo=O and Mo-O bond length decrease and Raman bands shift toward higher wavenumber when the transformation of anchoring site from single Al atom to double Al atoms takes places [32]. Consequently, it is implied that the shift to the high wavenumber with decreasing the Si/Al_2 ratio originates from the transformation of isolated Mo dioxo species anchored from single Al atom sites to double Al atom sites on the surface.

To further visualize the difference in Mo oxide dispersion of all Mo containing samples, the distribution of Mo was investigated by STEM-EDS analysis after pretreated at 680 ℃ for 0.5 h under He flow. Figure 2-6 indicates HAADF-STEM image and the corresponding EDS mapping analysis data for Mo over all the samples. It can be seen that dark contrasts, observed in the STEM image, are well matched with red spots in the corresponding EDS maps for Mo. In Figure 2-6, Mo(5)/H-MCM-22 (21) sample displays highly dispersed Mo particles. As Si/Al_2 ratio increases, Mo particles become agglomerated in patches and, finally, Mo(5)/H-MCM-22 (91) sample has the biggest Mo particles among the samples. Therefore, it certainly supports that the dispersion of Mo oxide is related to the change of BAS determined by Si/Al_2 ratio.

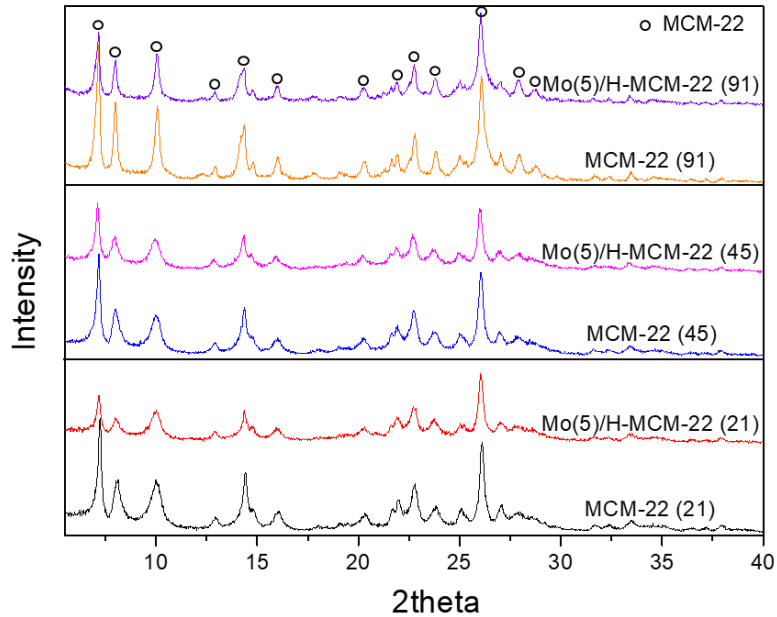

Figure 2-2. XRD patterns for MCM-22 and Mo(5)/H-MCM-22 samples with Si/Al_2 ratios of 21, 45 and 91.

Table 2-2. BET surface area, micropore volume and relative crystallinity of MCM-22 and Mo(5)/H-MCM-22 samples.

Catalyst	BET surface area (m^2/g)	Micropore volume (cm^3/g)	Relative Crystallinity (%)
MCM-22 (21)	570	0.191	100
MCM-22 (45)	565	0.191	96
MCM-22 (91)	406	0.144	108
Mo(5)/H-MCM-22 (21)	419	0.142	70
Mo(5)/H-MCM-22 (45)	433	0.143	63
Mo(5)/H-MCM-22 (91)	343	0.121	84

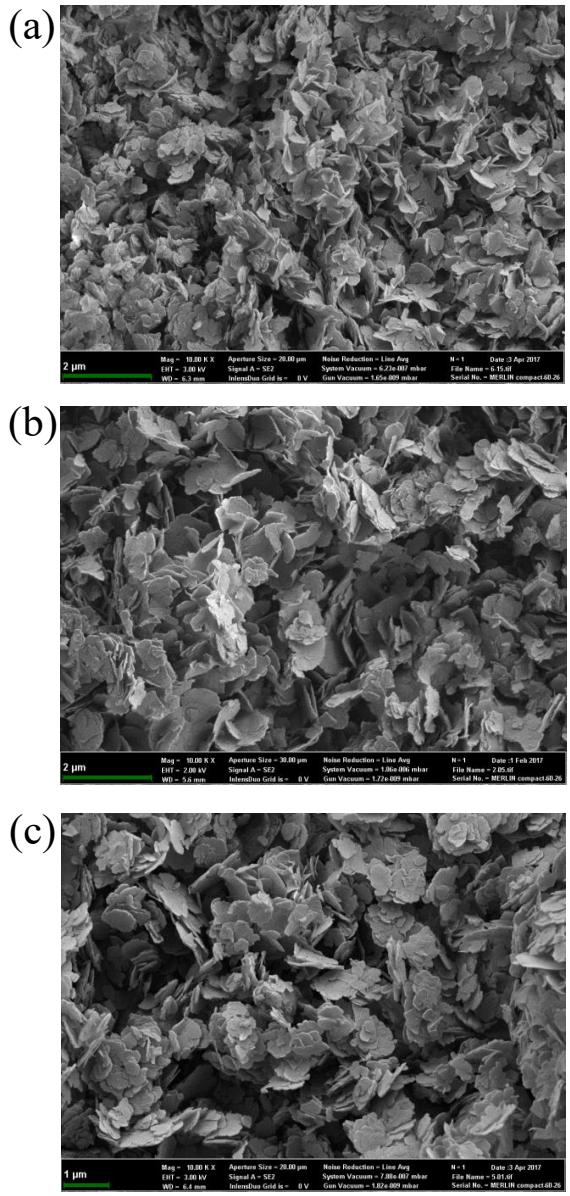

Figure 2-3. SEM images of MCM-22 zeolites with various Si/Al_2 ratios: (a) MCM-22 (21), (b) MCM-22 (45) and (c) MCM-22 (91).

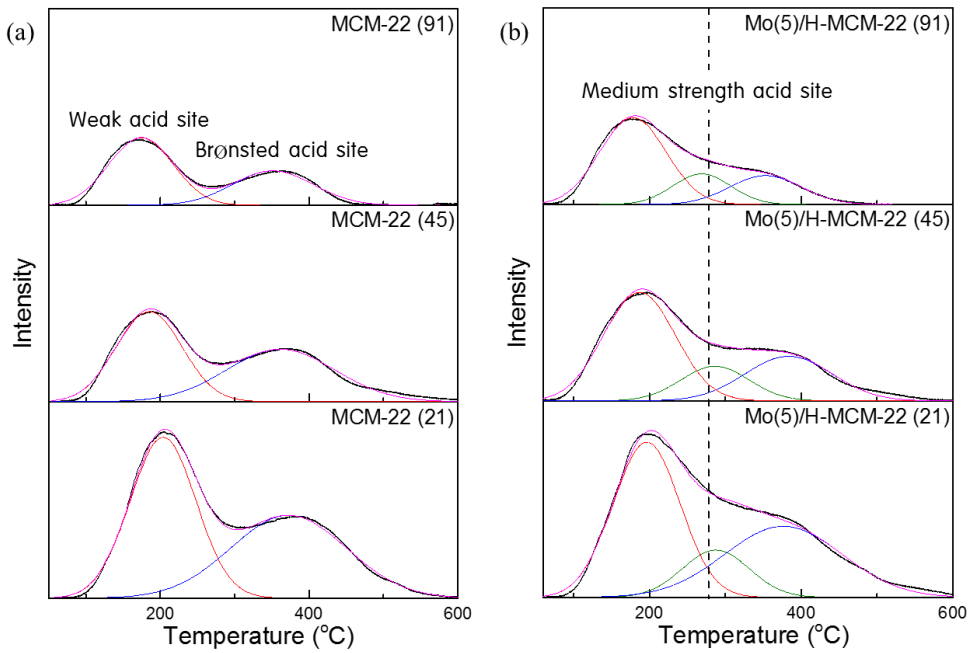

Figure 2-4. NH_3 TPD profiles of all (a) MCM-22 and (b) Mo(5)/H-MCM-22 catalysts.

Table 2-3. Peak position and amount of desorbed ammonia for NH_3 TPD profiles in MCM-22 and Mo(5)/H-MCM-22 catalysts with different Si/Al_2 ratios.

Catalyst	Peak position (℃)			Amount[a] (mmol/g)		
	WAS	MAS	BAS	WAS	MAS	BAS
MCM-22 (21)	192	-	369	0.884	-	0.799
MCM-22 (45)	184	-	361	0.485	-	0.488
MCM-22 (91)	175	-	350	0.361	-	0.246
Mo(5)/H-MCM-22 (21)	196	287	382	0.831	0.257	0.606
Mo(5)/H-MCM-22 (45)	188	285	383	0.632	0.193	0.316
Mo(5)/H-MCM-22 (91)	179	271	354	0.474	0.146	0.168

a: Amount of desorbed ammonia

Table 2-4. Surface atomic composition and Mo/(Si+Al) ratio of the Mo containing catalysts determined by XPS analysis.

Catalyst	Surface atomic composition (%)				Mo/(Si+Al) ratio
	Al	Mo	O	Si	
Mo(5)/H-MCM-22 (21)	2.38	0.91	63.37	33.34	$2.54 \cdot 10^{-2}$
Mo(5)/H-MCM-22 (45)	1.25	0.96	62.73	35.00	$2.65 \cdot 10^{-2}$
Mo(5)/H-MCM-22 (91)	0.82	1.20	62.11	35.87	$3.27 \cdot 10^{-2}$

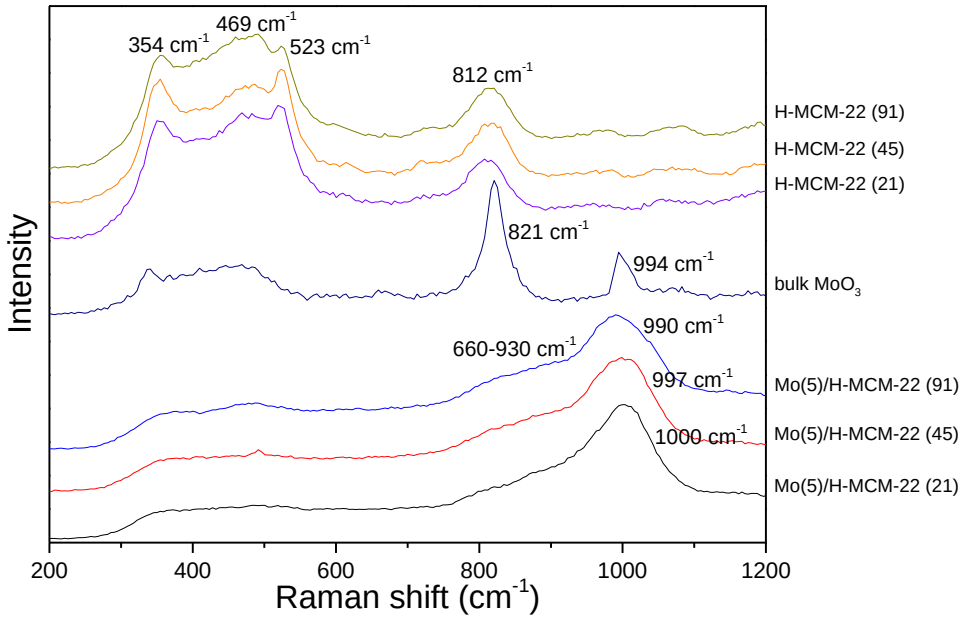

Figure 2-5. UV Raman spectra of bulk MoO_3, Mo(5)/H-MCM-22 and H-MCM-22 samples.

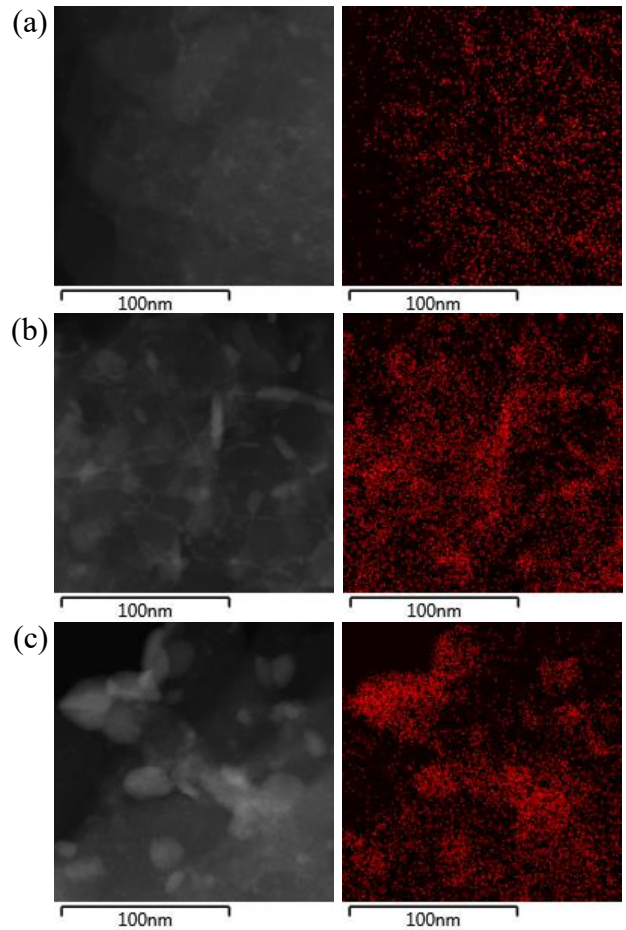

Figure 2-6. (Left) HAADF-STEM image and (Right) the corresponding EDS mapping analysis data for Mo of (a) Mo(5)/MCM-22 (21), (b) Mo(5)/MCM-22 (45) and (c) Mo(5)/MCM-22 (91).

2.3.2. Catalytic activity

The effect of Mo containing catalysts with various Si/Al_2 ratios on catalytic performance of MDA reaction was investigated at 680 ℃ under atmospheric pressure. The methane conversion rate, benzene formation rate, deactivation rate, selectivity of benzene, naphthalene and carbonaceous deposit for all the Mo(5)/H-MCM-22 catalysts are plotted with time on stream (TOS) in Figure 2-7(a)-(d). It is observed that the fast decline in methane conversion rate arises during the initial reaction stage less than 2 h, as shown in Figure 2-7(a). Such fast decline originating from methane decomposition results in the carburization of the molybdenum oxide to molybdenum carbide species like Mo_2C (or MoO_xC_y) which are known as an active site of methane activation. It is called as "induction period" [18, 50, 51]. The methane conversion rate of the Mo containing catalysts increases as the Si/Al_2 ratio decreases and, in particular, Mo(5)/H-MCM-22 (21) has the highest methane conversion rate among the catalysts. It is interesting to note that methane conversion rate continues to decline with TOS in all the catalysts, which signifies that deactivation of the catalysts continuously happens during the reaction.

Figure 2-7(b) indicates the benzene formation rate for the Mo(5)/H-MCM-22 catalysts plotted with TOS. It is observed that benzene formation rate decreases with increasing the Si/Al_2 ratio and the descending order is as follow: Mo(5)/H-MCM-22 (21) > Mo(5)/H-MCM-22 (45) > Mo(5)/H-MCM-22 (91). Such benzene formation rate of the Mo(5)/H-MCM-22 catalysts has similar tendency to their methane conversion rate, and, hence, it is considered that both rates can be influenced by a same factor.

Figure 2-7(c) shows the selectivity of benzene and naphthalene while Figure 2-7(d) shows the selectivity of carbonaceous deposit for all the Mo containing catalysts. Both figures exhibit low selectivity of benzene and high selectivity of carbonaceous deposit for all the Mo containing catalysts at the early stage of reaction since this region belongs to an induction period. After this period, the selectivity of benzene increases while that of carbonaceous deposit decreases. In case of benzene selectivity, Mo(5)/H-MCM-22 (21) has 51.9% and 42.6% of benzene selectivity at TOS of 2 and 13 h, respectively, which exhibits the highest selectivity among the samples. On the other hand, Mo(5)/H-MCM-22 (91) has 36.1% and 7.5% of benzene selectivity at TOS of 2 and 13 h, respectively, which shows the lowest selectivity among the samples. In addition, in case of carbonaceous deposit selectivity, Mo(5)/H-MCM-22 (21) has 34.4% and 44.6% of carbonaceous deposit selectivity at TOS of 2 and 13 h, respectively, which indicates the lowest selectivity among the samples. On the contrary, Mo(5)/H-MCM-22 (91) has 51.1% and 82.7% of carbonaceous deposit selectivity at TOS of 2 and 13 h, respectively, which shows the highest selectivity among the samples. Here, naphthalene selectivity of all the samples is below about 7% throughout the whole reaction time, which is quite lower than that of Mo containing ZSM-5 catalyst because of smaller the pore size of MCM-22 (4.0 × 5.0 Å, 4.0 × 5.5 Å) than ZSM-5 (5.1 × 5.5 Å, 5.3 × 5.6 Å) [22, 52]. To sum up, the selectivity of benzene decreases while that of carbonaceous deposit increases with increasing not only TOS but also Si/Al_2 ratio. Therefore, once the Si/Al_2 ratio decreases, benzene formation is enhanced at the expense of carbonaceous deposits in MDA reaction.

In order to compare the extent of deactivation for catalysts, deactivation rate is obtained by applying a linear fitting method to benzene formation rate, as presented in Figure 2-7(b). The range of TOS is selected between 2 and 6.7 h since the region of TOS less than 2 h is an induction period region and that of TOS longer than 6.7 h is severe deactivation region of Mo(5)/H-MCM-22 (91) indicating that the benzene formation rate almost converges to zero point. Figure 2-7(b) shows that the ascending order of the deactivation rate is as follows: Mo(5)/H-MCM-22 (21) ($-0.336 \cdot 10^{-1}$ mmol/($g_{cat} \cdot h^2$)) < Mo(5)/H-MCM-22 (45) ($-0.353 \cdot 10^{-1}$ mmol/($g_{cat} \cdot h^2$)) < Mo(5)/H-MCM-22 (91) ($-0.404 \cdot 10^{-1}$ mmol/($g_{cat} \cdot h^2$)). As a result, Mo(5)/H-MCM-22 (21) catalyst has the lowest deactivation rate, in other words, it has the highest stability in the MDA reaction among all the catalysts.

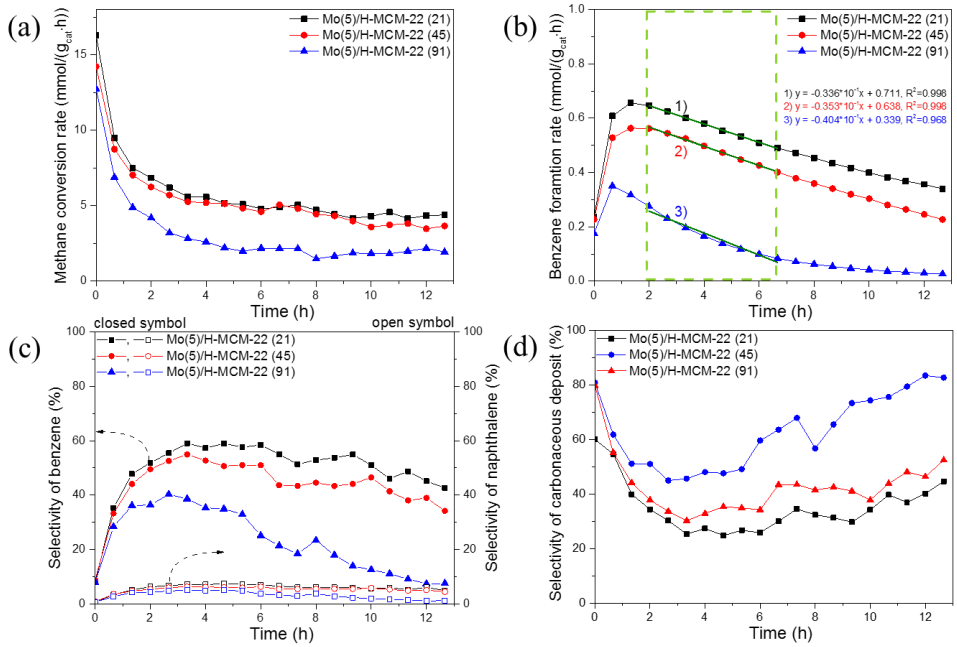

Figure 2-7. Catalytic performance of all Mo(5)/H-MCM-22 catalysts: (a) methane conversion rate, (b) benzene formation rate and 1) - 3) deactivation rate measured as a function of slope calculated by applying a linear fitting method to benzene formation rate, (c) selectivity of benzene and naphthalene and (d) selectivity of carbonaceous deposit.

2.3.3. Characterization of post-reaction catalysts

Figure 2-8 shows the TPO profiles of the Mo containing catalysts after running the reaction for 13 h. The profiles can be de-convoluted to the low temperature peak at 535-562 ℃ and the high temperature peak at 607-636 ℃ denoted as LT type and HT type coke, respectively. The peak position with maximum CO_x formation and amount of two type cokes are listed in Table 2-5. As shown in Figure 2-8, the peak position of LT type coke shifts toward higher temperature and its peak broadens as Si/Al_2 ratio decreases. It is attributed to the carbonaceous deposit associated with molybdenum (such as Mo_2C or MoO_xC_y) and carbidic carbon in molybdenum carbide (such as external molybdenum carbide particle) [33, 53]. Tempelman et al. insisted the gradual transformation of the molybdenum carbide phase from highly dispersed molybdenum carbide particles (Mo_2C or MoO_xC_y) to large agglomerated ones (external molybdenum carbide particle) with increasing TOS [34]. Such transformations of LT type coke may be related to the presence of Mo oxides on the surface because large agglomerated molybdenum carbide particles are easily formed when the amount of Mo oxides is larger on the surface. Moreover, it is reported that the peak position of LT type coke shifts toward lower temperature and its peak sharpens as the amount of Mo oxides is larger [33]. Thus, peak shift to low temperature and sharpening of peak may be attributed to the agglomeration of Mo oxide particles at the external surface of zeolite rather than the dispersion of Mo oxides into microchannel of zeolite, which eventually signifies that Mo(5)/H-MCM-22 (21) sample has a high dispersion of Mo oxides into microchannel of zeolite. On the other hand, although it is observed that the amount of LT type coke varies

depending on the Si/Al_2 ratios, it is not regarded as an essential deactivation factor since it does not hinder the activation of methane [21].

HT type coke is constituted of polyaromatics type cokes on BAS mainly located at the external surface of zeolite [34]. It is noteworthy that the amount of HT type coke increases as follows: 17.0 mg/g_{cat} of Mo(5)/H-MCM-22 (21) < 21.1 mg/g_{cat} of Mo(5)/H-MCM-22 (45) < 35.6 mg/g_{cat} of Mo(5)/H-MCM-22 (91). According to the results of deactivation rate and carbonaceous deposit selectivity, the degree of deactivation of the catalysts decreases as the Si/Al_2 ratio decreases, which is well matched with the trend for the amount of HT type coke. Consequently, HT type coke is regarded as a main deactivation factor for MDA reaction.

Figure 2-9 indicates TPO profiles of carbonaceous deposit derived from the dehydrogenation of naphthalene adsorbed on MCM-22, which is obtained in the following: naphthalene is adsorbed on MCM-22 with Si/Al_2 ratios of 21, 45 and 91 and then the resulting samples are calcined at 400 ℃ for 3 h under air condition. It is observed that the peak at 225 ℃ can be attributed to the sublimation of residual naphthalene and the peak at about 600 ℃ can be corresponding to carbonaceous deposit derived from the dehydrogenation of naphthalene. The peak at high temperature in Figure 2-9 is similar to that of HT type coke for post-reaction catalysts. In accordance with the results, the amount of carbonaceous deposit increases with increasing BAS, which shows that carbonaceous deposit derived from naphthalene can be mainly located at the BAS of zeolite.

As shown in Figure 2-10, UV Raman analysis was applied to shed further light on chemical species on the surface of zeolite over the post-reaction samples [54].

Compared to fresh catalysts, the Raman spectra of the post-reaction catalysts exhibit that the bands of fresh Mo(5)/H-MCM-22 catalysts, at 660-930 and ~995 cm^{-1}, almost disappear while new bands at 1400, 1480 and 1610 cm^{-1} appear. Previous studies suggested that new bands are assigned to several types of carbon formed during the reaction [54, 55]. The Raman spectra of polyaromatics (such as naphthalene, biphenyl and anthracene) and graphite were obtained to investigate the kind of carbonaceous deposits in the post-reaction catalysts as exhibited in Figure 2-10. The new bands are in agreement with the bands of naphthalene and anthracene (a sharp peak at 1610 cm^{-1} and two small peaks at 1400 and 1480 cm^{-1}). Thus, the surface of Mo(5)/H-MCM-22 samples is mostly covered by the HT type coke consisting of carbonaceous deposits mainly derived from polyaromatics such as naphthalene and anthracene.

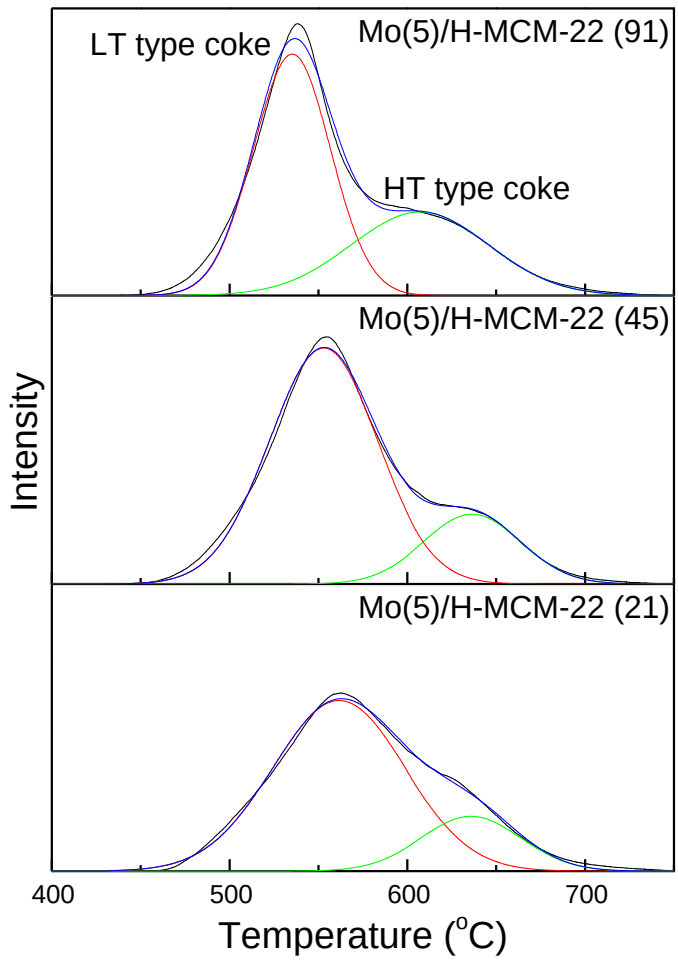

Figure 2-8. TPO profiles of Mo containing catalysts after running the reaction for 13 h.

Table 2-5. Peak position and amount of coke for TPO profiles of Mo containing catalysts after running the reaction for 13 h.

Catalyst	Peak position (°C)		Amount of coke (mg/g_{cat})	
	LT type	HT type	LT type	HT type
Mo(5)/H-MCM-22 (21)	562	636	68.5	17.0
Mo(5)/H-MCM-22 (45)	554	636	76.8	21.1
Mo(5)/H-MCM-22 (91)	535	607	56.8	35.6

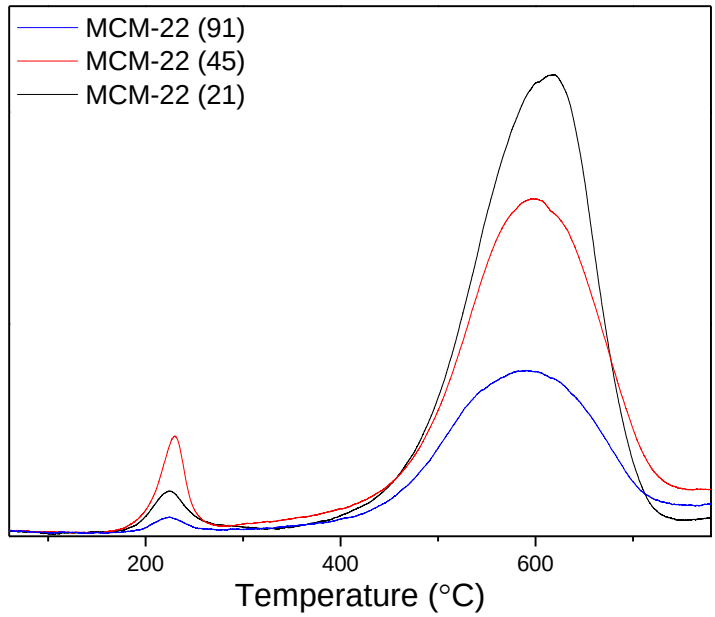

Figure 2-9. TPO profiles of carbonaceous deposit derived from the dehydrogenation of naphthalene adsorbed on MCM-22.

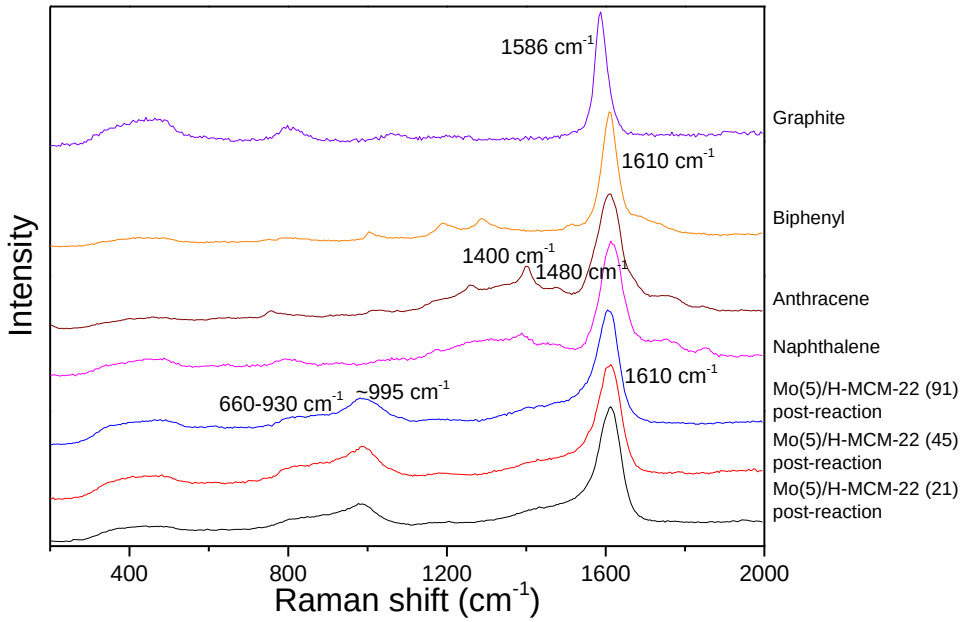

Figure 2-10. UV Raman spectra of post-reaction catalysts and reference samples.

2.4. Discussion

Combined XPS, TPO and UV Raman analysis indicates that the amount of Mo atom and polymeric Mo oxide species decreases on the surface of zeolite as the Si/Al_2 ratio decreases, which confirms that Mo oxides are well dispersed. Moreover, it is shown that the dispersion of Mo oxides is proportional to the amount of BAS. Such trend of the dispersion of Mo oxides was visually demonstrated by comparative STEM-EDS analysis of each samples. Consequently, it is evidently proved that BAS stabilizes monomeric Mo oxide species, by facilitating to migrate Mo oxides from the surface into the microchannel of zeolite since the amount of BAS is quite larger inside the micropore than on the external surface.

Mo(5)/H-MCM-22 (21) and Mo(5)/H-MCM-22 (45) sample are compared to examine the effect of textural property of MCM-22 samples on dispersion of Mo oxides. It is verified that although both zeolites have an almost identical textural properties, their dispersions of Mo oxides are different from each other. Hence, we can exclude the possibility of having an effect of textural property of zeolite on the dispersion of Mo oxides.

In accordance with the activity and characterization results, it is clearly confirmed that methane conversion and benzene formation rate increase as the dispersion of Mo oxides increases. It evidently indicates that high dispersion of Mo oxides can contribute to the formation of well dispersed Mo_2C (or MoO_xC_y) species during induction period. On the other hand, Tessonnier et al. claimed that higher performance of ZSM-5 catalysts with low Si/Al_2 ratios is mainly ascribed to the

different anchoring mode of the molybdenum [31]. UV Raman results indicate that the increment in Raman shift may give rise to the transformation of anchoring site from single Al atom to double Al atoms as the Si/Al_2 ratio decreases. In particular, Mo(5)/H-MCM-22 (21) may possess the highest distribution of isolated Mo dioxo species anchored to double Al atom sites as evidenced by their high wavenumber shift. Therefore, high distribution of isolated Mo dioxo species anchored to double Al atom sites might contribute to improving the activity and stability of catalyst for MDA reaction.

According to the TPO and UV Raman analysis of post-reaction catalysts, and the deactivation rate results, HT type coke is mostly composed of polyaromatics like naphthalene and anthracene. The formation of HT type coke increases as the amount of BAS decreases, which points out that it is proportional to the amount of Mo oxides present on the surface. In addition, the amount of HT type coke is proportional to the deactivation rate during MDA reaction. Hence, low dispersion of Mo oxides can accelerate the formation of HT type coke, leading to rapid deactivation of catalyst.

The main reason for the deactivation of catalyst may be the blockage of channel by the production of HT type coke. Some researchers proposed that the formation of carbonaceous deposit derived from polyaromatics at the external zeolite surface reduces the micropore volume and crystallinity of the catalysts [33, 34]. Thus, it is expected that the formation of HT type coke on the micropore openings brings about decreased accessibility of methane inside the micropores, which eventually reduces the activity for MDA reaction.

Most studies suggested the bifunctional activation mechanism for MDA reaction where ethylene, produced by dehydrogenation and coupling of methane at Mo_2C (or MoO_xC_y), is oligomerized to benzene on the BAS in the microchannel of zeolite [18, 27]. If oligomerization of ethylene mainly occurs on the BAS of external surface of zeolite under MDA reaction condition, main product would be polyaromatics because of the absence of shape selectivity on the external surface. Then, HT type coke may be formed resulting from the dehydrogenation of polyaromatics at the external surface of zeolite and its amount would be proportional to that of BAS, as exhibited in Figure 2-9. For this reason, we compared the formation of HT type coke to shed light on the role of BAS related to oligomerization. To sum up, it is expected that the formation of HT type coke is proportional to the amount of BAS when oligomerization of ethylene occurs on the BAS of external surface of zeolite [37, 38]. However, the formation of HT type coke is proportional to the amount of Mo oxides present on the external surface in accordance with our results. Consequently, activity for MDA reaction can be primarily affected by the dispersion of Mo oxides, which is different from the suggested bifunctional activation mechanism. Here, we cannot completely exclude the possibility that acid sites are also involved in ethylene conversion reactions. Therefore, it may be suggested that activation mechanism for MDA reaction is primarily monofunctional mechanism, mainly originating from well dispersed molybdenum carbides inside the microchannel of zeolite with shape selectivity.

Chapter 3. Characteristics of Mn/H-ZSM-5 catalysts for methane dehydroaromatization

3.1. Introduction

Methane, as the most abundant hydrocarbon resource, is a main constituent of natural gas and shale gas. It has attracted substantial attention as an alternative energy resource, which can be converted to more valuable hydrocarbon products through a direct method under nonoxidative condition. The direct method is advantageous in that it has a lower cost and shorter operation time than the indirect method, which involves a two-step process [56]. In addition, the conversion of methane under nonoxidative condition is believed to be promising, because it has a higher selectivity of desired products than that under oxidative condition. Among the reactions under nonoxidative conditions, the MDA reaction is more thermodynamically favorable for converting methane into benzene than other products, so it has attracted considerable attention [2].

To date, various transition metals (such as Mo, Re, W, Zn, and Mn) loaded on ZSM-5 have been studied in order to identify a catalyst with excellent activity of MDA reaction [13-16]. Among the active metals with which to activate methane, manganese oxide has great potential for the MDA reaction, because manganese is the most abundant and cheapest. For example, Lee and Oyama suggested that the manganese oxide catalyst activated the C-H bond of methane under oxidative conditions [57]. Borodko et al. reported that the manganese oxide catalyst converted methane into C2-hydrocarbons under nonoxidative conditions [58]. In addition,

Marczewski and Marczewska proposed that methane is converted to light hydrocarbons over MnO_x loaded on SiO_2 and SiO_2-Al_2O_3 catalysts under nonoxidative condition [59]. Using this methane activation property of manganese oxide, Tan et al. applied manganese supported ZSM-5 catalyst to the MDA reaction at the reaction temperature above 700 °C [14]. As the reaction temperature increases to 800 °C, although aromatic compounds were produced, the deactivation of the catalyst was accelerated. It was also suggested that Mn_3O_4, as a precursor of the active phase for methane activation, was carburized during the MDA reaction, thus affecting methane activity. However, it is somewhat controversial to insist that Mn_3O_4 is an active phase precursor for MDA reaction without detailed analysis of manganese species, because various manganese species such as isolated Mn^{2+} ion, isolated Mn^{3+} ion, MnO, Mn_2O_3, Mn_3O_4, and MnO_2 can exist in Mn/ZSM-5 catalyst [60-62]. Therefore, it is necessary to investigate the effects of various manganese species in Mn/H-ZSM-5 catalyst on the MDA reaction.

In this study, we aimed to investigate the effects of various manganese species on the MDA reaction by changing the loading amount of Mn. Furthermore, we attempted to identify the activation and deactivation mechanisms of Mn/H-ZSM-5 catalyst by elucidating the characteristics of the catalysts as the reaction proceeds.

3.2. Experimental

3.2.1. Catalysts preparation

The commercial NH_4-ZSM-5 (Alfa Aesar) with a Si/Al_2 ratio of 23 was used after calcination at 500 ℃ for 4 h in order to obtain the H-ZSM-5 form. Mn was loaded on the H-ZSM-5 using an incipient wetness impregnation method with an aqueous solution of manganese (II) acetate tetrahydrate as a metal precursor at room temperature. The resulting samples were dried at 105 ℃ overnight, and then calcined in a muffle furnace at 500 ℃ for 4 h. The synthesized catalysts were designated as Mn(X)/H-ZSM-5 catalysts, where X is the wt % of Mn loaded on the H-ZSM-5. The Mn(X)/H-ZSM-5 catalysts were analyzed after being treated at 750 ℃ for 0.5 h under Ar flow in order to simulate the pretreatment condition.

Post-reaction samples were prepared through the following procedure. The catalyst was pretreated to 750 ℃ for 0.5 h in an Ar flow rate of 20 ml/min. Then, the catalyst was evaluated at 750 ℃ with a 10% He/CH_4 gas mixture in a flow rate of 10 ml/min with various time-on-stream, followed by rapid cooling down to room temperature with Ar flow. The resulting catalysts are designated as Mn(5)/H-ZSM-5 (Pretreated), Mn(5)/H-ZSM-5 (10 min), Mn(5)/H-ZSM-5 (50 min), Mn(5)/H-ZSM-5 (130 min), Mn(5)/H-ZSM-5 (290 min), and Mn(5)/H-ZSM-5 (850 min).

3.2.2. Catalysts characterization

Powder X-ray diffraction (XRD) analysis was conducted with a SmartLab (Rigaku) with Cu Kα radiation at 30 mA and 40 kV. The XRD patterns were collected in a 2θ range from 5 º to 75 º with a scanning step size of 0.02 º at a speed of 2 º/min.

Inductively coupled plasma-atomic emission spectroscopy (ICP-AES), ICPS-8100 (Shimadzu), was applied in order to obtain an actual loading amount of Mn in Mn(X)/H-ZSM-5 samples.

N_2 physisorption was performed on a BELSORP-mini II (BEL Japan). Prior to measurement, all catalysts were degassed under evacuated conditions at 250 ℃ for at least 10 h. BET surface area and pore volume were calculated using the Brunauer-Emmett-Teller (BET) and t-plot methods, respectively.

The temperature programed desorption of NH_3 (NH_3 TPD) was carried out using a thermal conductivity detector (TCD) in a BEL-CAT BASIC (BEL Japan Inc.). To begin, 0.05 g of sample loaded on quartz wool in a U-shaped quartz tube was pretreated under He flow at 400 ℃ for 1 h, then cooled down to 120 ℃. Afterward, the sample was exposed to 5% NH_3/He gas at 120 ℃ for 1 h, then purged under He flow at 120 ℃ for 1 h in order to remove weakly adsorbed NH_3 molecules from the surface. Next, the sample was heated to 800 ℃ with He flow at a rate of 10 ℃/min.

Temperature programed reduction by H_2 (H_2 TPR) was conducted on a TCD in a BEL-CAT-II (MicrotracBEL, Corp.) instrument. Prior to analysis, 0.03 g of catalyst was heated to 400 ℃ for 1 h in a flow of 21% O_2/N_2. The catalyst was then cooled down to 40 ℃ and stabilized under 5% H_2/Ar for 30 min. Afterward, the sample was heated to 900 ℃ with 5% H_2/Ar flow at a rate of 10 ℃/min.

X-ray photoelectron spectroscopy (XPS) spectra were collected on a K-alpha (Thermo Scientific Inc., U.K.); the instrument uses a 400 μm-diameter beam and a focused monochromatic Al Kα X-ray (1486.6 eV) source operated at 36 W. The binding energy scale was calibrated using the Si 2p at 103.3 eV.

In situ DRIFT analysis was carried out on a Nicolet 6700 (Thermo Fisher Scientific) equipped with an MCT detector and a high temperature DRIFT cell with ZnSe windows. DRIFT spectra were recorded in the 4000-400 cm^{-1} range with 64 scans at a resolution of 4 cm^{-1}. Prior to the analysis, the samples packed in the DRIFT cell were pretreated in 10% O_2/N_2 (100 mL/min) at 500 °C for 1 h in order to remove impurities. The cell was then cooled down to 300 °C and stabilized for at least 10 min with 10% O_2/N_2 (100 mL/min), after which spectra were obtained. The background spectra of KBr were acquired in this step.

UV Raman spectra were collected in the 200–2000 cm^{-1} range using a Renishaw (In Via Raman Microscope) with a CCD detector. The instrument uses a 244 nm line of an Ar laser as an excitation source.

Temperature programed oxidation (TPO) was carried out on a BEL-CAT-II (MicrotracBEL, Corp.) with a TCD. Without pretreatment, 0.03 g of sample was heated to 800 °C with 5% O_2/He flow at a heating rate of 5 °C/min. CO and CO_2 are the main products, because H_2O was removed by an H_2O trap during the oxidation. The detection curves for both products have shapes similar to each other, in accordance with the previous report [9]. Therefore, CO_x (the amounts of CO and CO_2) can only be used as a produced species during TPO.

3.2.3. Catalytic activity measurement

The catalytic test for the MDA reaction was conducted under atmospheric pressure in a fixed-bed quartz reactor. At first, for the reaction test, 0.2 g of catalyst was sieved to a size between 425 and 850 μm. The catalyst was preheated to 750 ℃ and kept for 0.5 h in an Ar flow rate of 20 ml/min. Then, 10% He/CH_4 gas mixture was fed to the reactor at a flow rate of 10 ml/min.

The reactant and reaction products were analyzed every 40 minutes using an on-line gas chromatograph (YL6500GC) equipped with two columns (Carboxen-1000 column and GS-Gaspro) and two detectors (thermal conductivity detector and flame ionization detector). The outlet pipeline was maintained at 230 ℃ in order to avoid condensation and adsorption of the hydrocarbon products in the pipeline. By using a helium gas as an internal standard, the methane conversion rate, selectivity of various products, and carbonaceous deposits were calculated based on carbon mass balance [63].

3.3. Results

3.3.1. Characterization of fresh catalysts

The crystalline structures of H-ZSM-5 and Mn(X)/H-ZSM-5 samples were investigated through XRD analysis. Figure 3-1 indicates that the XRD patterns of the Mn(X)/H-ZSM-5 samples have peaks assigned to those of the H-ZSM-5 sample, in accordance with previous studies [13, 64]. It can be seen that the XRD patterns arising from manganese species do not appear even though the amount of Mn is loaded up to 10wt%. In order to examine the change in the crystallinity of H-ZSM-5 as a function of the various loading amounts of Mn, the relative crystallinities of the samples were calculated using the intensity of the largest peak at 2θ of 23.1°. Table 3-1 shows the relative crystallinities of the Mn(X)/H-ZSM-5 samples with the Mn loading amounts of 0wt%, 2.5wt%, 5wt%, 7.5wt% and 10wt% is 100%, 75%, 65%, 57%, and 50%, respectively. Thus, it can be seen that although crystallite patterns for manganese species are absent, the relative crystallinity of zeolite decreases with increasing loading amounts of Mn. Hence, the amount of manganese species that are highly dispersed or having small particle size below the detection limit of XRD increases with the loading amount of Mn.

The BET surface areas and micropore/total volumes of H-ZSM-5 and Mn(X)/H-ZSM-5 catalysts were measured by N_2 physisorption, as listed in Table 3-1. When the loading amount of Mn increases, it is shown that BET surface area and total pore volume decrease from 318 to 241 m^2/g and from 0.196 to 0.159 cm^3/g, respectively.

As a result, the BET surface area and micropore volume decrease with increasing loading amounts of Mn.

NH_3 TPD analysis was used to estimate the amount of acid sites in H-ZSM-5 and Mn(X)/H-ZSM-5 samples. NH_3 TPD profiles of all of the samples are displayed in Figure 3-2. The H-ZSM-5 sample has two desorption peaks at 201 ℃ and 380 ℃. The former peak is assigned to the desorption of NH_3 species located at non-exchangeable cationic sites, referred to as weak acid site (WAS). By contrast, the latter peak is attributed to the desorption of NH_3 species adsorbed on exchangeable protonic sites, denoted as the Brønsted acid site (BAS) [38, 65, 66]. When Mn is loaded on H-ZSM-5, the amount of BAS decreases while a new peak originating from the medium strength acid site (MAS) appears at about 250 ℃ [22].

The amounts of desorbed ammonia from the acid sites of the samples are summarized in Table 3-2. As the loading amount of Mn increases, the amounts of not only BAS but also overall acid sites decrease. Here, the decrease in the amount of BAS arises from the ion exchange of Mn^{2+} ions at BAS of H-ZSM-5 [60]. When the loading amount of Mn reaches up to 5wt%, the amount of BAS decreases significantly with further increasing loading amounts of Mn. However, as the loading amount of Mn exceeds 5wt%, a decrease in the amount of BAS becomes moderate with further increasing loading amount of Mn. Such a slight reduction in BAS may be regarded as a decrease in the amount of overall acid sites because of a decrease in surface area with increasing loading amount of Mn. In summary, as the loading amount of Mn is above 5wt%, the amount of Mn^{2+} ions to anchor to BAS remains almost constant.

H_2 TPR analysis was applied in order to examine the oxidation state of Mn in Mn(X)/ZSM-5 catalysts. H_2 TPR profiles of the catalysts are presented in Figure 3-3. Mn(X)/H-ZSM-5 catalysts with Mn loading amounts higher than 5wt% have broad reduction peaks at lower temperature (about 386 ℃) and sharp reduction peaks at higher temperature (about 484 ℃), designated as α and β peaks, respectively. The α peak can be ascribed to the reduction from isolated Mn^{3+} ion and amorphous MnO_x species to Mn^{2+} species [60, 62]. Although the reduction of amorphous MnO_x is suggested as α peak according to previous studies, that possibility is excluded in this study. If the amorphous MnO_x species is present, it is expected to increase with increasing loading amounts of Mn. However, the H_2 consumption for α peak is hardly changed with increasing loading amounts of Mn. Hence, the α peak can only be ascribed to the reduction from isolated Mn^{3+} ion species bound at the anchoring site of zeolite, rather than the reduction from amorphous MnO_x. Meanwhile, a previous study proposed that the β peak can be assigned to the reduction of Mn^{3+} in agglomerated Mn_2O_3 species to Mn^{2+} species [62].

The H_2 consumptions for the α and β peaks of the samples are summarized in Table 3-3. They show a different trend with increasing loading amounts of Mn. In the case of α peak, the Mn(2.5)/H-ZSM-5 catalyst has a very small H_2 consumption (0.012 mmol/g) while Mn(5), Mn(7.5), and Mn(10)/H-ZSM-5 catalysts have rather constant H_2 consumption (about 0.110 mmol/g). In the case of β peak, Mn(2.5)/H-ZSM-5 catalyst has no H_2 consumption. Mn(5), Mn(7.5), and Mn(10)/H-ZSM-5 catalysts have 0.006, 0.129, and 0.236 mmol/g of H_2 consumption, respectively. Consequently, as the loading amount of Mn exceeds 5wt%, the amount of isolated Mn^{3+} species

remains at approximately 0.110 mmol/g, while that of agglomerated Mn_2O_3 species increases considerably.

The reduction from Mn^{2+} in MnO species to Mn metal species is not observed up to 900 ℃, as shown in Figure 3-3, which means that the reduction potential from Mn^{2+} in MnO to Mn metal species has a large negative value [67, 68]. Based on the fact that all species are reduced to MnO and Mn^{2+} ion species under 900 ℃, the oxidation state of Mn and composition of Mn species were calculated, as displayed in Table 3-3. Mn^{2+} ion species is produced by an ion exchange of Mn^{2+} ion with BAS and MnO species that can be formed by the reduction of Mn_2O_3 during high temperature pretreatment under Ar. It can be seen that the amount of Mn^{2+} ion and MnO species increases with increasing loading amounts of Mn.

XPS analysis for Mn 2p was performed in order to ascertain the oxidation state of Mn on the surface of zeolite for Mn(X)/H-ZSM-5 samples. Mn 2p photoelectron spectra of Mn(X)/H-ZSM-5 and bulk Mn_xO_y samples are shown in Figure 3-4 and Figure 3-5, respectively. It is quite challenging to differentiate the oxidation state between Mn^{2+} and Mn^{3+} ion, because the variation of BE is very small, specifically less than 0.2 eV, as indicated in Figure 3-5 [69]. Accordingly, the XPS analysis of the samples was carried out in comparison with that obtained from bulk reference samples. The binding energy (BE) for Mn 2p and Mn/(Si+Al) ratio on the surface for the Mn(X)/H-ZSM-5 samples are summarized in Table 3-4. The Mn(2.5)/H-ZSM-5 sample has the highest BE of 643.0 eV for Mn $2p_{3/2}$ among the catalysts. The Mn(5), Mn(7.5), and Mn(10)/H-ZSM-5 samples have BE of 642.3, 641.9, and 641.7 eV for Mn $2p_{3/2}$, respectively. Hence, when the loading amount of Mn increases, the

BE for Mn $2p_{3/2}$ decreases and approaches 641.5 eV, which is attributed to BE for Mn $2p_{2/3}$ in reference MnO and Mn_2O_3.

As shown in Table 3-4, the ratios of Mn/(Si+Al) increase as the loading amount of Mn increases, and, in particular, the Mn(10)/H-ZSM-5 sample has the highest Mn/(Si+Al) ratio among the samples. The Mn/(Si+Al) ratio implies the relative amount of Mn atom located on the surface of zeolite since XPS is a surface analysis technique. Therefore, it can be summarized that when the loading amount of Mn increases, the amount of Mn_xO_y drastically increases on the surface of zeolite.

As indicated in Figure 3-6, DRIFT analysis was conducted in order to examine the anchoring site of Mn to ZSM-5 in all Mn(X)/H-ZSM-5 catalysts by comparing the characteristic bands arising from surface hydroxyl groups. In the range of 4000-3200 cm^{-1}, three characteristic bands for surface hydroxyl groups can be observed. The first band at 3602 cm^{-1} originates from Bronsted acid sites (Si-OH-Al), while the second band at 3653 cm^{-1} and the third band at 3740 cm^{-1} are assigned to hydroxyl groups on extra-framework Al sites (ex-Al-OH) and terminal Si sites (Si-OH), respectively [32, 70]. When the loading amount of Mn is 2.5wt%, the band for Si-OH-Al group is considerably reduced. This means that Mn^{2+} ions are preferentially ion-exchanged in BAS as Mn is loaded on H-ZSM-5. When the loading amount of Mn is 5wt%, the band for not only the Si-OH-Al group, but also the ex-Al-OH and Si-OH groups, are reduced, implying that the ex-Al-OH and Si-OH groups can also serve as anchoring sites for Mn^{2+} ions, corresponding well to the previous report indicating that other metals such as Mo and Cr were also anchored to ex-Al-OH and

Si-OH groups [32, 71]. However, when the loading amount of Mn exceeds 5wt%, all bands of surface hydroxyl groups are not changed.

In the range of 1100-875 cm^{-1}, a new band appears as Mn is loaded on H-ZSM-5. The new band at 957 cm^{-1} is attributed to the change in T-O-T vibrations of the zeolite framework because of the local perturbation by Mn^{2+} ions anchored to BAS [60, 72]. The intensity of the new band increases up to 5wt% of Mn loading, while it is hardly changed when the loading amount of Mn is above 5wt%. Consequently, the increase in new band has a similar tendency to the reduction of the band for Si-OH-Al group, which evidently demonstrates that Mn^{2+} ions are anchored to BAS. It can be summarized that when Mn is loaded on H-ZSM-5, Mn^{2+} ions are preferentially ion-exchanged with BAS, then anchored to ex-Al-OH and Si-OH groups with increasing Mn loading.

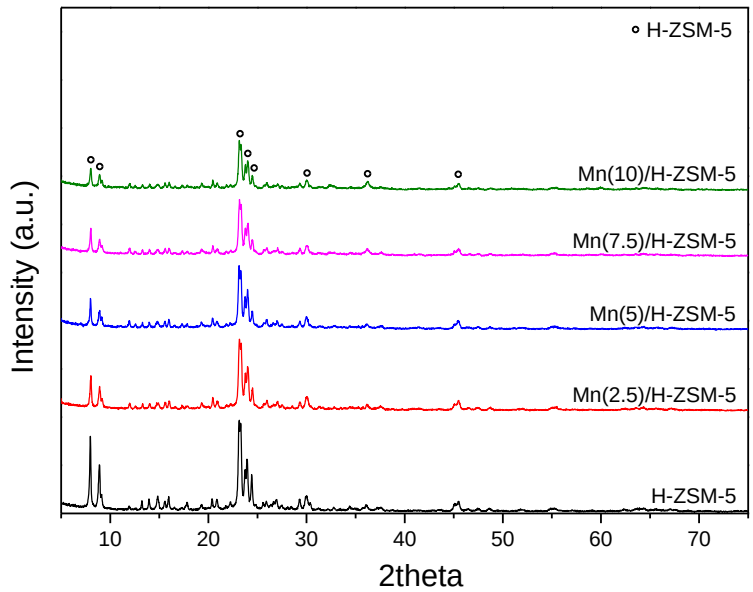

Figure 3-1. XRD patterns for H-ZSM-5 and Mn(X)/H-ZSM-5 samples.

Table 3-1. Amounts of Mn, BET surface areas, micropore/total volumes, and relative crystallinities of H-ZSM-5 and Mn(X)/H-ZSM-5 catalysts.

Catalyst	Amount of Mn (ICP AES)	BET SA (m^2/g)	Micropore V /Total V (cm^3/g)	Relative Crystallinity (%)
H-ZSM-5	-	318	0.150/0.196	100%
Mn(2.5)/H-ZSM-5	2.5wt%	284	0.131/0.178	75%
Mn(5)/H-ZSM-5	4.8wt%	263	0.123/0.169	65%
Mn(7.5)/H-ZSM-5	7.1wt%	251	0.115/0.163	57%
Mn(10)/H-ZSM-5	9.2wt%	241	0.111/0.159	50%

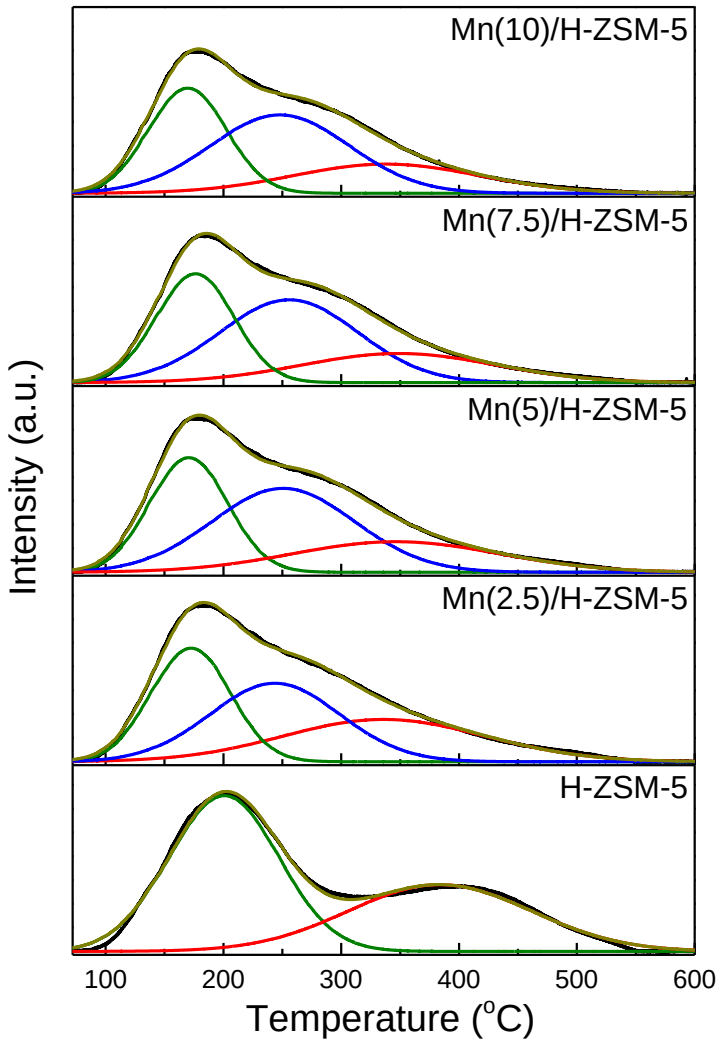

Figure 3-2. NH_3 TPD profiles of H-ZSM-5 and Mn(X)/H-ZSM-5 samples.

Table 3-2. Peak positions and amounts of desorbed ammonia obtained from NH_3 TPD profiles of H-ZSM-5 and Mn(X)/H-ZSM-5 samples.

Catalyst	Peak position (℃)			Amount of desorbed NH_3 (mmol/g)			
	WAS	MAS	BAS	WAS	MAS	BAS	Total
H-ZSM-5	201	-	380	0.809	-	0.674	1.483
Mn(2.5)/H-ZSM-5	172	244	337	0.446	0.509	0.424	1.379
Mn(5)/H-ZSM-5	170	251	346	0.441	0.594	0.311	1.346
Mn(7.5)/H-ZSM-5	176	257	351	0.412	0.564	0.282	1.258
Mn(10)/H-ZSM-5	170	248	342	0.401	0.541	0.268	1.210

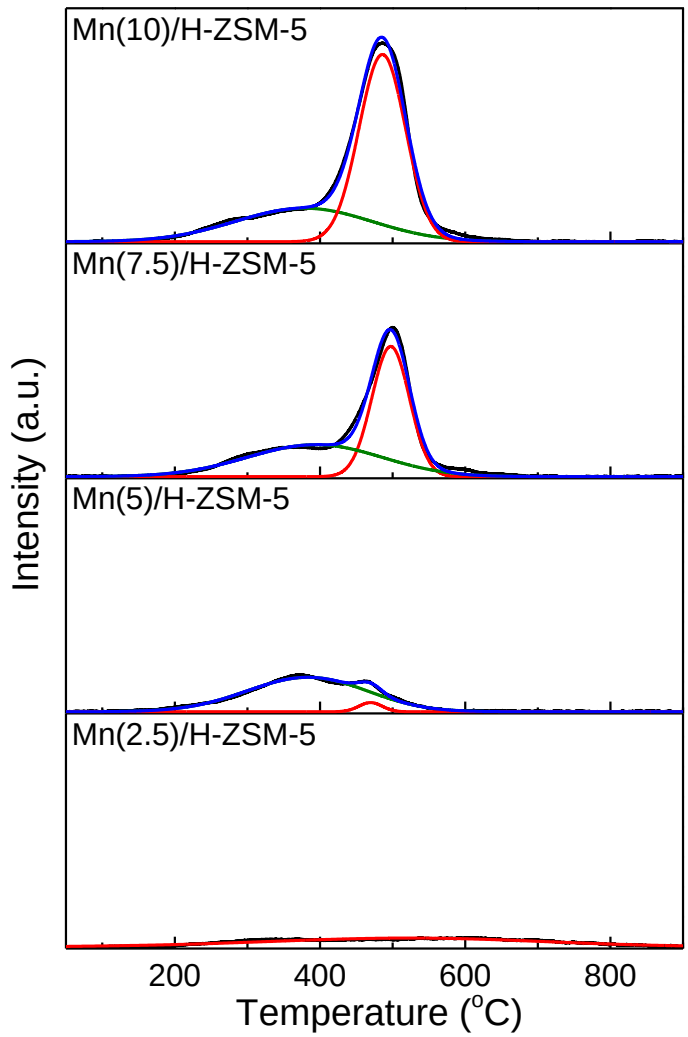

Figure 3-3. H_2 TPR profiles of Mn(X)/ZSM-5 catalysts.

Table 3-3. Peak positions and H_2 consumptions obtained from H_2 TPR profiles of Mn(X)/ZSM-5 catalysts.

Catalyst	Peak position (℃)		H_2 consumption (mmol/g)		Oxidation state of Mn	Composition of Mn species (%)		
	α	β	α	β		Mn^{3+}	Mn_2O_3	Mn^{2+} and MnO
Mn(2.5)/H-ZSM-5	400	-	0.012	-	2.05	5%	-	95%
Mn(5)/H-ZSM-5	384	470	0.108	0.006	2.26	24%	2%	74%
Mn(7.5)/H-ZSM-5	394	497	0.110	0.129	2.37	17%	20%	63%
Mn(10)/H-ZSM-5	379	486	0.111	0.236	2.42	14%	28%	58%

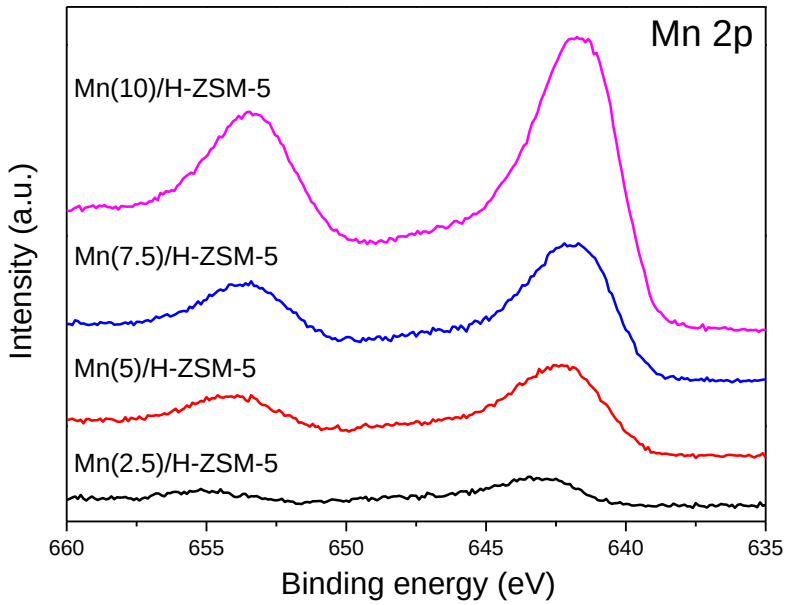

Figure 3-4. XPS spectra for Mn 2p of Mn(X)/H-ZSM-5 samples.

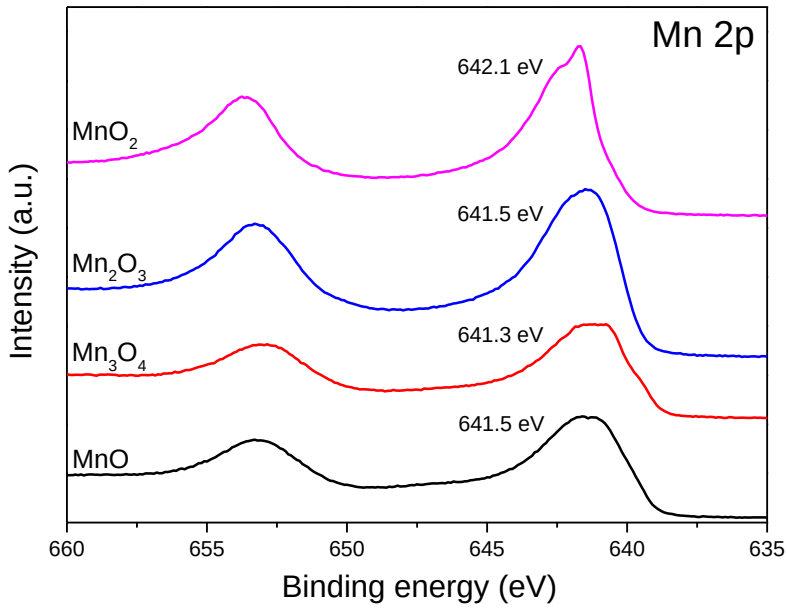

Figure 3-5. XPS spectra for Mn 2p of bulk Mn_xO_y samples.

Table 3-4. Binding energy of Mn 2p and Mn/(Si+Al) ratio of Mo containing catalysts obtained from XPS analysis.

Catalyst	BE of Mn $2p_{1/2}$ (eV)	BE of Mn $2p_{3/2}$ (eV)	Mn/(Si+Al) Ratio
Mn(2.5)/H-ZSM-5	655.1	643.0	1.6
Mn(5)/H-ZSM-5	654.0	642.3	5.3
Mn(7.5)/H-ZSM-5	653.5	641.9	10.0
Mn(10)/H-ZSM-5	653.3	641.7	24.9

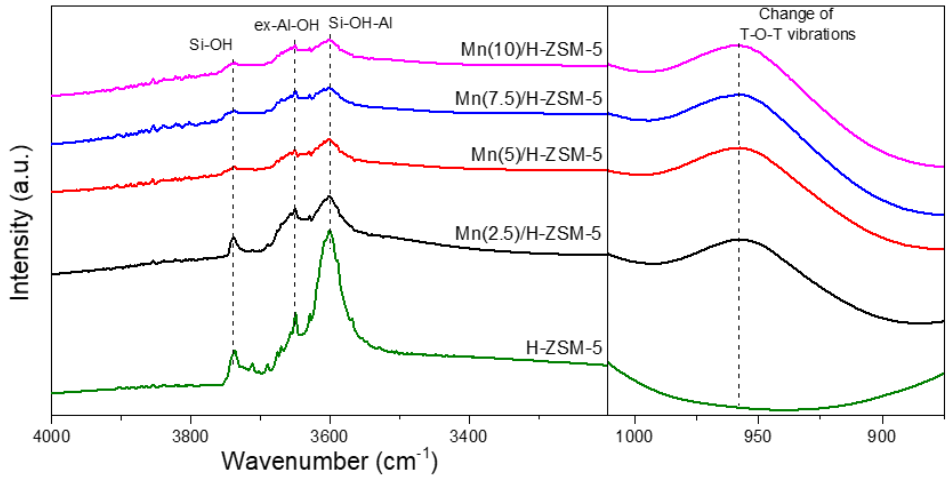

Figure 3-6. DRIFT spectra of H-ZSM-5 and Mn(X)/H-ZSM-5 catalysts.

3.3.2. Catalytic activity

The catalytic performance of the MDA reaction over Mn(X)/H-ZSM-5 samples was evaluated at 750 ℃ under atmospheric pressure. Figure 3-7(a) indicates the methane conversion rate for Mn(X)/H-ZSM-5 catalysts plotted with time-on-stream (TOS). The methane conversion rate largely increases when the loading amount of Mn increases up to 5wt%; however, as the loading amount of Mn exceeds 5wt%, the methane conversion rate starts to decrease. Thus, the descending order of methane conversion rates is as follows: Mn(5)/H-ZSM-5 > Mn(7.5)/H-ZSM-5 > Mn(10)/H-ZSM-5 > Mn(2.5)/H-ZSM-5. On the other hand, it is observed that the methane conversion rate continually decreases with increasing TOS after passing the time with the highest methane conversion rate in all samples. This underlines that deactivation of the catalyst steadily occurs as the reaction proceeds.

Figure 3-7(b) shows the benzene formation rate for the samples plotted with TOS. The benzene formation rate increases as the loading amount of Mn increases, and, in particular, the Mn(5)/H-ZSM-5 sample has the highest benzene formation rate among the samples. However, when the loading amount of Mn exceeds 5wt%, the formation rate of benzene decreases, which is a similar tendency to that of the change of methane conversion rate.

Figure 3-7(c) indicates the benzene and naphthalene selectivities and Figure 3-7(d) shows the ethylene and carbonaceous deposit selectivities for the samples plotted with TOS. In the cases of benzene and naphthalene selectivities, the Mn(5)/H-ZSM-5 sample shows the highest selectivity among the samples. It has 50.4% and 22.5% of benzene and naphthalene selectivities at TOS of 130 min, which decrease to 28.1%

and 6.7% at TOS of 850 min, respectively. By contrast, the Mn(2.5)/H-ZSM-5 sample exhibits the lowest selectivity among the samples. It has 36.7% and 13.0% of benzene and naphthalene selectivities at TOS of 130 min, which decreases to 11.0% and 3.6% at TOS of 850 min, respectively. In the cases of ethylene and carbonaceous deposit selectivities, the Mn(5)/H-ZSM-5 sample shows the lowest selectivity among the samples. It has 4.0% and 5.8% of ethylene and carbonaceous deposit selectivities at TOS of 130 min, which increases to 14.3% and 40.5% at TOS of 850 min, respectively. On the other hand, the Mn(2.5)/H-ZSM-5 sample shows the highest selectivity among the samples. It has 9.9% and 27.8% of ethylene and carbonaceous deposit selectivities at TOS of 130 min, which increases to 18.4% and 59.5% at TOS of 850 min, respectively. In summary, the Mn(5)/H-ZSM-5 sample having the highest activity exhibits the maximum values of benzene and naphthalene selectivities and the minimum value of ethylene and carbonaceous deposit selectivities.

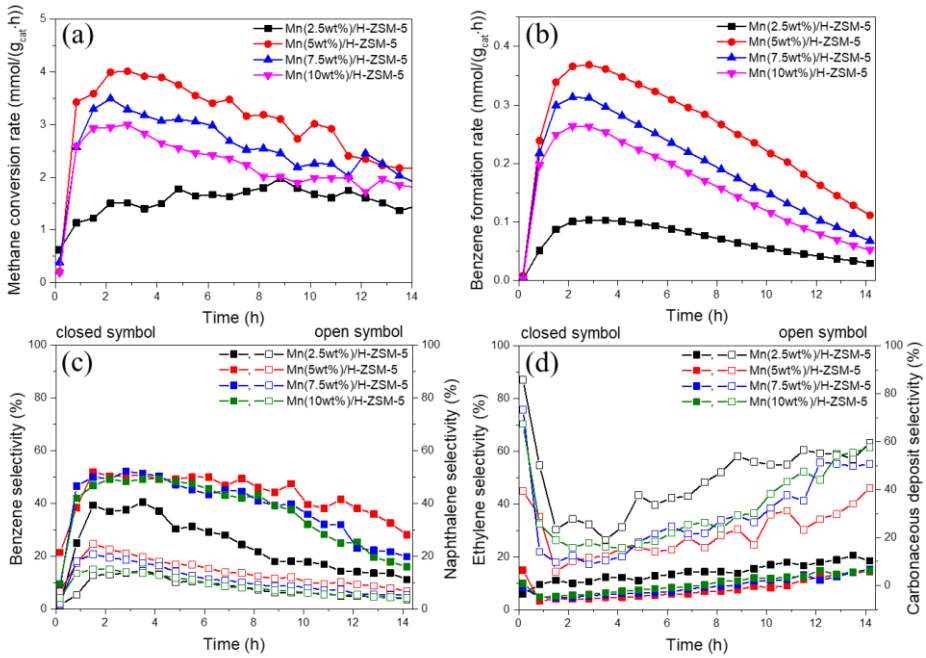

Figure 3-7. Catalytic performance of Mn(X)/H-ZSM-5 samples: (a) methane conversion rate, (b) benzene formation rate, (c) benzene and naphthalene selectivities and (d) ethylene and carbonaceous deposit selectivities.

3.3.3. Characterization of post-reaction catalysts

Table 3-5 shows the BET surface areas and micropore/total volumes of post-reaction catalysts with different TOS obtained from N_2 physisorption. The Mn(5)/H-ZSM-5 (Pretreated) sample has a BET surface area of 263 m^2/g and a micro pore volume of 0.123 cm^3/g. Until TOS of 130 min, both values slightly decrease to 242 m^2/g of BET surface area and 0.113 cm^3/g of micro pore volume. As TOS exceeds 130 min, both values decrease significantly and approach 113 m^2/g and 0.052 cm^3/g at TOS of 850 min. Consequently, new chemical species produced during the reaction diminish the BET surface area and micro pore volume.

The XRD patterns for post-reaction catalysts with different TOS are shown in Figure 3-8, and their relative crystallinities are listed in Table 3-5. Until TOS of 130 min, relative crystallinity slightly decreases to 88% and is almost maintained up to 850 min. Hence, the structure of zeolite is hardly collapsed, even after TOS of 850 min.

UV Raman analysis of the standard and post-reaction samples was applied in order to prove the chemical species on the surface of zeolite produced during the MDA reaction. UV Raman analysis can avoid fluorescence interference and enhance the Raman band intensity due to a resonance effect [45]. Such a resonance phenomenon happens because the characteristic bands associated with isolated transition metal and several carbonaceous deposit species have absorption bands between the 200 and 300 nm region, which is close to the laser excitation source of 244 nm [54]. As shown in Figure 3-9, H-ZSM-5 demonstrates Raman bands at 395, 467, 815, 1090, and 1214 cm^{-1}, which is in agreement with the reported Raman bands of MFI zeolite

[73, 74]. Among these bands, the strongest band at 395 cm^{-1} can be assigned to the five-membered ring vibration of the ZSM-5 framework [73]. When Mn is loaded on H-ZSM-5, the Raman bands of H-ZSM-5 decrease, whereas a new Raman band appears at 651 cm^{-1}, attributed to a stretching vibration of Mn-O-Mn species [75]. As the reaction proceeds, the Raman bands of Mn(5)/H-ZSM-5 (Pretreated) are maintained up to TOS of 130 min. Once TOS exceeds 130 min, however, the intensity of the Raman bands decreases and eventually, disappears after TOS of 850 min. By contrast, a new Raman band appears at about 1590 cm^{-1} after TOS of 130 min. This band becomes larger and sharper as the reaction proceeds. It is expected that the new band is one of the carbonaceous deposit species (such as polyaromatics and graphite) formed during the MDA reaction [76]. According to the results of UV Raman analysis for naphthalene and graphite reference samples, it is confirmed that the new Raman band is well matched with the Raman band of graphite (a sharp peak at 1586 cm^{-1}). Thus, as the reaction proceeds, the surface of Mn(5)/H-ZSM-5 becomes covered with graphite-like species, which may be attributed to the graphitic carbon associated with manganese species or carbidic carbon in manganese carbide (or oxycarbide) [77].

XPS analysis of post-reaction catalysts with different TOS was performed in order to determine which species were produced during the MDA reaction. XPS spectra for C 1s and Mn 2p of the post-reaction catalysts are presented in Figure 3-10(a) and (b) respectively. In Figure 3-10(a), the XPS spectra for C 1s indicate that the post-reaction catalysts have a peak located at a BE of about 284.8 eV. According to previous studies, a BE of about 283 eV is attributed to the carbidic carbon species

and a BE of 284.8 eV is assigned to the graphitic carbon species [18, 69]. Hence, it can be clearly seen that the carbonaceous deposits are mainly present as graphitic carbon species rather than as carbidic carbon species in the post-reaction catalysts. In addition, the XPS spectra for Mn 2p exhibit that the post-reaction catalysts possess a peak located at about 642.3 eV. Borodko et al. proposed that the shoulder peak at BE of 641 eV appeared after the OCM reaction at 850 ℃ under nonoxidative condition, which may be attributed to surface manganese carbide [58]. Consequently, it is confirmed that surface manganese carbide (or oxycarbide) is not formed during the MDA reaction, since the peaks of XPS spectra for Mn 2p are not shifted to low BE during the reaction.

The relative surface atomic concentrations of post-reaction catalysts obtained from XPS analysis are listed in Table 3-6. The surface atomic percent of carbon remains at about 20% up to TOS of 130 min. However, as TOS exceeds 130 min, the surface atomic percent of carbon increases up to 62% at TOS of 850 min. Thus, it is evident that the surface of catalyst is gradually covered with carbon as the reaction proceeds.

TPO analysis was conducted in order to investigate the state of carbonaceous deposit species formed during the MDA reaction. Figure 3-11 exhibits TPO profiles of all of the post-reaction catalysts with different TOS. The TPO result of Mn(5)/H-ZSM-5 (Pretreated) shows a negative peak, in other words, the consumption of oxygen, even without the progression of the MDA reaction. In order to confirm how the chemical states of manganese change based on O_2 consumption peak during TPO, H_2 TPR analysis of all of the fresh Mn(X)/H-ZSM-5 catalysts was evaluated after pretreatment at 400 ℃ for 1h in a flow of 21% O_2/N_2 or N_2 gas, as shown in Figure

3-12. It is noted that TPR analysis with pretreatment using 21% O_2/N_2 gas is the same as that shown in Figure 3-3. In the case of pretreatment using N_2 gas, the result of H_2 TPR indicates that the isolated Mn^{3+} ion species is completely reduced and the agglomerated Mn_2O_3 species is slightly reduced, as compared to the case of using 21% O_2/N_2 gas. Thus, pretreatment using 21% O_2/N_2 gas mainly oxidizes isolated Mn^{2+} ion to isolated Mn^{3+} ion species, which underlines the fact that O_2 consumption peak in TPO analysis can be relevant to the oxidation of isolated Mn^{2+} ion to isolated Mn^{3+} ion species. Furthermore, the amount of H_2 consumption in the α peak of H_2 TPR is compared with the amount of O_2 consumption in the negative peak of TPO over all Mn(X)/H-ZSM-5 catalysts. H_2 consumption must be multiplied by two in consideration of the stoichiometry, so that it is described as $2H_2$ consumption. As indicated in Figure 3-13, the Mn(2.5)/H-ZSM-5 sample has a very small amount of O_2 consumption (0.023 mmol/g), while the Mn(5), Mn(7.5), and Mn(10)/H-ZSM-5 samples have similar amounts of O_2 consumption (approximately 0.221 mmol/g) to each other. In accordance with Table 3-7, it is confirmed that the amount of O_2 consumption at the negative peak of TPO is almost identical to that of $2H_2$ consumption at the α peak of H_2 TPR in all Mn(X)/H-ZSM-5 catalysts. Hence, it is clearly demonstrated that the negative peak is assigned to the oxidation of isolated Mn^{2+} ion to isolated Mn^{3+} ion species. As presented in Table 3-7, the O_2 consumption of the negative peak slightly decreases from 0.218 to 0.175 mmol/g up to TOS of 50 min. When TOS passes 130 min, this O_2 consumption significantly decreases to 0.068 mmol/g and finally becomes zero in the case of the sample after TOS of 850 min.

On the other hand, a new peak is observed at around 505 ℃ in TOS of 130 min. When the reaction proceeds, the intensity of the new peak increases and the oxidation temperature of the peak shifts to higher temperatures (from 505 to 557 ℃), indicating that the particle size grows [33]. The new peak, denoted as LT type coke, can be ascribed to the oxidation of carbonaceous deposit related to carbidic carbon in manganese carbide (or oxycarbide) or graphitic carbon related to active manganese species [33, 76, 78]. However, the formation of carbidic carbon is excluded according to the result of current XPS analysis suggesting that carbidic carbon species is not present. Thus, this change for the new peak can imply that active manganese species becomes covered with carbonaceous deposit due to the continued carburization, which leads to the formation of excessive carbonaceous deposit species on the catalyst.

Table 3-5. BET surface areas, micropore/total volumes and relative crystallinities of post-reaction catalysts with different time on stream.

Catalyst	BET SA (m^2/g)	Micropore V /Total V (cm^3/g)	Relative Crystallinity (%)
Mn(5)/H-ZSM-5 (Pretreated)	263	0.123/0.169	100%
Mn(5)/H-ZSM-5 (10 min)	252	0.117/0.165	92%
Mn(5)/H-ZSM-5 (50 min)	242	0.113/0.157	88%
Mn(5)/H-ZSM-5 (130min)	242	0.113/0.154	88%
Mn(5)/H-ZSM-5 (290min)	229	0.107/0.145	88%
Mn(5)/H-ZSM-5 (850min)	113	0.052/0.074	89%

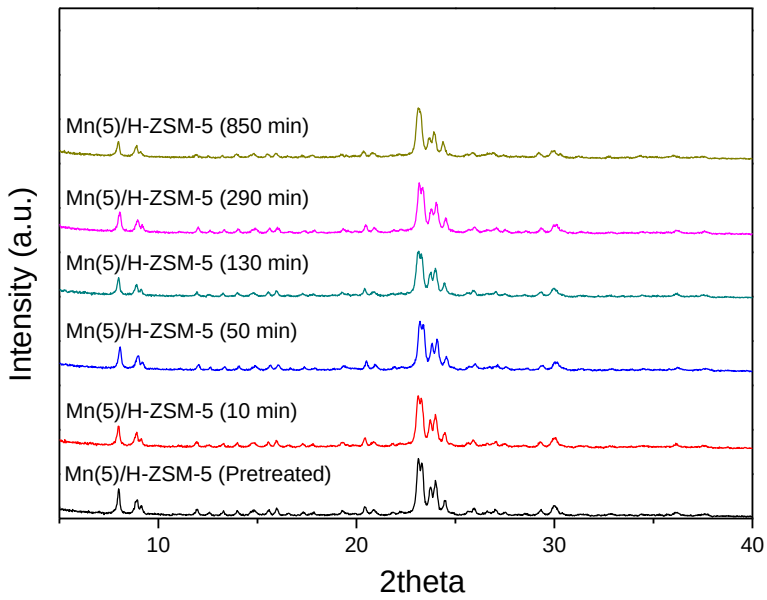

Figure 3-8. XRD patterns for post-reaction catalysts with different time on stream.

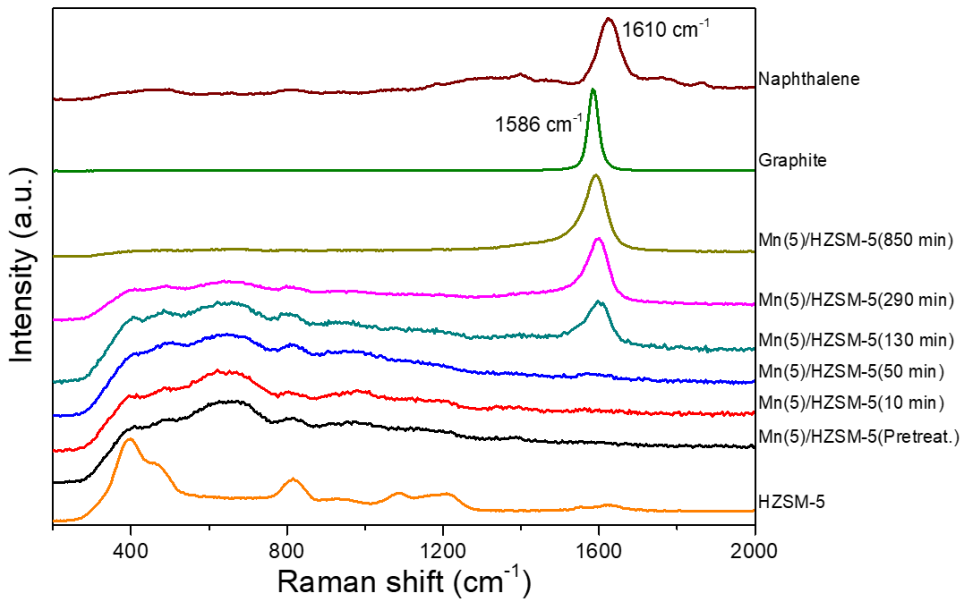

Figure 3-9. UV Raman spectra of standard and post-reaction samples.

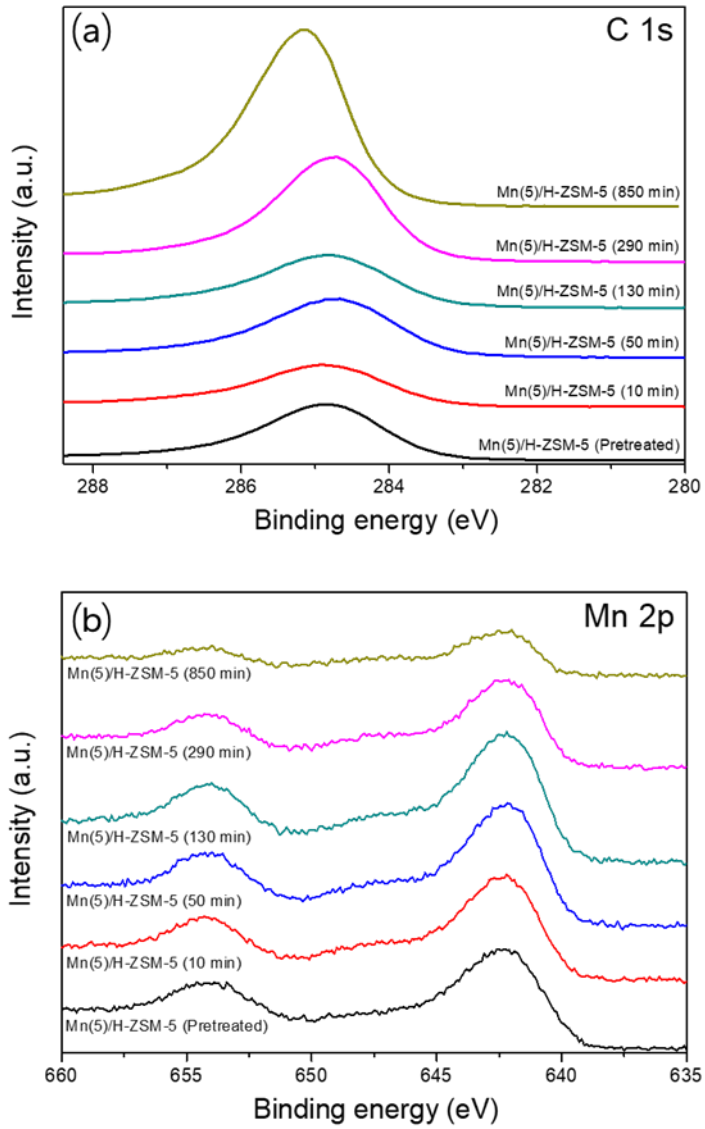

Figure 3-10. XPS spectra for (a) C 1s and (b) Mn 2p of post-reaction catalysts with different time on stream.

Table 3-6. Relative surface atomic concentrations obtained from XPS analysis of post-reaction catalysts with different time on stream.

Catalyst	Relative surface atomic concentration (%)				
	Al	C	Mn	O	Si
Mn(5)/H-ZSM-5 (Pretreated)	2.6	22.5	1.5	45.8	27.5
Mn(5)/H-ZSM-5 (10 min)	2.7	17.3	1.5	50.1	28.4
Mn(5)/H-ZSM-5 (50 min)	2.6	21.4	1.7	47.2	27.1
Mn(5)/H-ZSM-5 (130min)	2.6	20.0	1.8	48.7	27.0
Mn(5)/H-ZSM-5 (290min)	2.0	38.1	1.3	37.5	21.2
Mn(5)/H-ZSM-5 (850min)	1.3	62.4	0.7	23.8	11.8

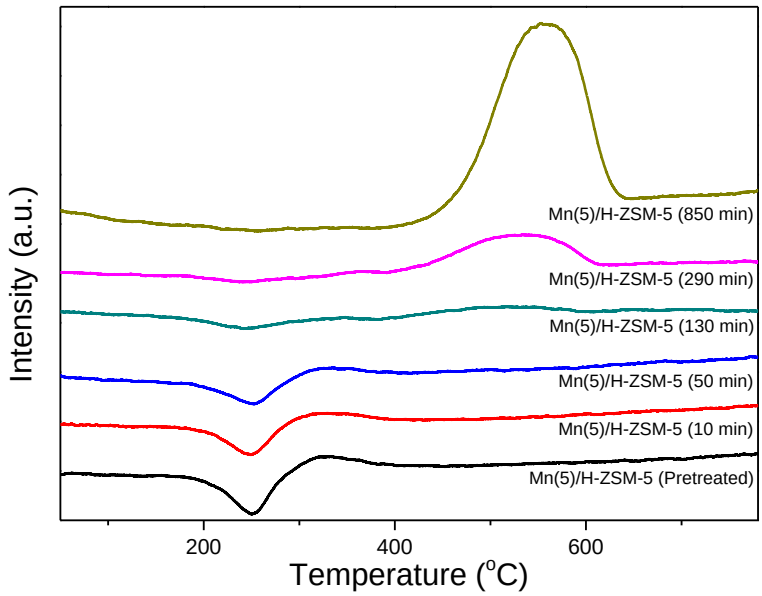

Figure 3-11. TPO profiles of the post-reaction catalysts with different time on stream.

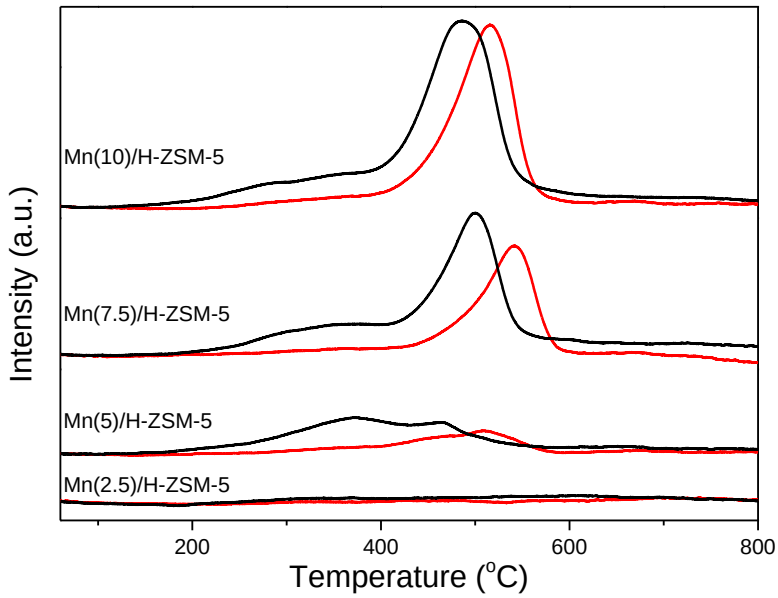

Figure 3-12. H_2 TPR profiles of Mn(X)/H-ZSM-5 catalysts analyzed at 400 ℃ for 1h by adjusting the pretreatment gas. 1) 21% O_2/N_2 – Black line and 2) N_2 – Red line

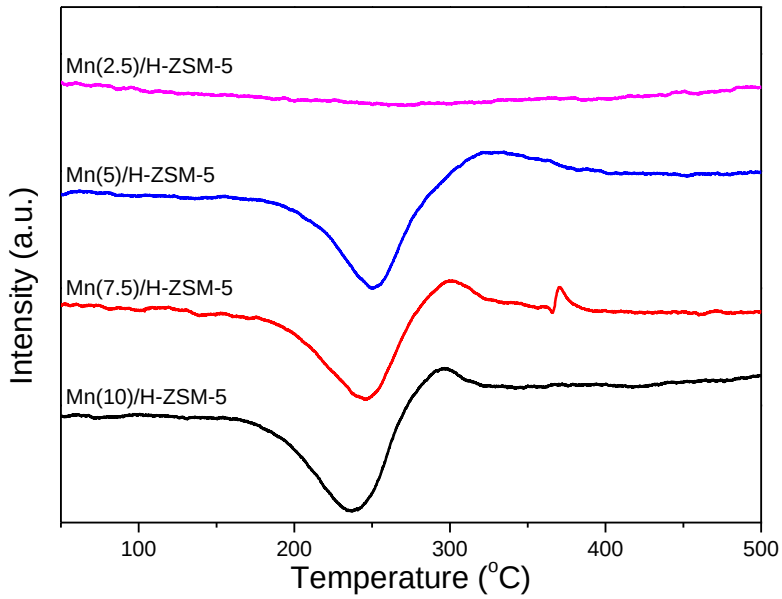

Figure 3-13. TPO profiles of Mn(X)/H-ZSM-5 catalysts.

Table 3-7. Peak position and O_2 consumption of negative peak from TPO profiles and $2H_2$ consumption of α peak from H_2 TPR profiles in Mn(X)/H-ZSM-5 and post-reaction catalysts.

Catalyst	Peak position (℃)	O_2 consumption[a] (mmol/g)	$2H_2$ consumption[b] (mmol/g)
Mn(2.5)/H-ZSM-5	271	0.023	0.024
Mn(5)/H-ZSM-5	251	0.218	0.216
Mn(7.5)/H-ZSM-5	246	0.219	0.220
Mn(10)/H-ZSM-5	240	0.225	0.222
Mn(5)/H-ZSM-5 (10 min)	248	0.198	-
Mn(5)/H-ZSM-5 (50 min)	252	0.175	-
Mn(5)/H-ZSM-5 (130min)	242	0.068	-
Mn(5)/H-ZSM-5 (290min)	242	0.043	-
Mn(5)/H-ZSM-5 (850min)	-	-	-

a: O_2 consumption of negative peak calculated from TPO result

b: $2\times H_2$ consumption of α peak calculated from H_2 TPR result

3.4. Discussion

Combined H_2 TPR and NH_3 TPD analysis shows the presence of several manganese species, such as isolated Mn^{2+} ion, isolated Mn^{3+} ion, agglomerated MnO, and agglomerated Mn_2O_3 species, depending on the loading of Mn. The reason that several manganese species are produced can be demonstrated by DRIFT analysis. The result of DRIFT analysis clearly indicates that solvated Mn^{2+} ions are preferentially ion-exchanged in BAS at the Mn loading of 2.5wt%. Because the ion-exchanged Mn^{2+} ion in BAS is strongly bonded, it still exists as Mn^{2+} ion species without changing the oxidation state, even after calcination and pretreatment, which is in agreement with the results of H_2 TPR and NH_3 TPD analysis. Mn^{2+} ions can be ion-exchanged with H-ZSM-5 as Mn^{2+}, $Mn(OH)^+$, and $[Mn\text{-}O\text{-}Mn]^{2+}$ ion species [60]. As shown in Table 3-8, the results of the repeated ion exchange step with 0.1 M $Mn{\cdot}(CH_3COO)_2{\cdot}4H_2O$ aqueous solution indicate that the amount of Mn converges to 2.43 wt% when ion exchange is repeated three times. This means that such a value is the maximum loading amount of Mn that can be ion-exchanged in BAS of H-ZSM-5. If the Mn^{2+} ion is ion-exchanged with two H^+ ions at BAS, the theoretical amount of Mn that can be ion-exchanged at BAS of H-ZSM-5 with a Si/Al_2 ratio of 23 is less than 3.1wt%, which is calculated by the amount of Al present in H-ZSM-5 (23) via ICP analysis. Therefore, Mn^{2+} ion will be mainly ion-exchanged with two BAS among the Mn^{2+} ions.

When the available BAS are consumed by ion exchange of Mn^{2+} ion with BAS, the solvated Mn^{2+} ions become anchored to the ex-Al-OH and Si-OH groups at the Mn

loading of 5wt%. Such anchoring can be attributed to the electrostatic interaction between manganese cations in $Mn(H_2O)_6$ complex and hydroxyl groups (ex-Al-OH and Si-OH) [79]. Following the calcination and pretreatment procedure, isolated Mn^{2+} ion anchored on both hydroxyl groups is oxidized to Mn^{3+} ion species [80].

As the available hydroxyl groups are consumed by the anchoring of Mn^{2+} ion to the ex-Al-OH and Si-OH groups, the remaining solvated Mn^{2+} ions are deposited as the $Mn(H_2O)_6$ complex at the Mn loadings at 7.5 and 10wt% [79]. Since there is no interaction with the surface hydroxyl groups, such manganese complex species can be agglomerated on the external surface of zeolite during the pretreatment with high temperature, which results in the formation of agglomerated MnO and Mn_2O_3 species. Therefore, isolated Mn^{2+} ion and isolated Mn^{3+} ion species are mainly formed by the anchoring of Mn^{2+} ion to BAS and hydroxyl groups (ex-Al-OH and Si-OH) in zeolite, respectively, at the Mn loading below 5wt%, whereas agglomerated MnO and Mn_2O_3 is formed on the external surface of zeolite without anchoring to any sites at the Mn loading above 5wt%.

In order to determine which species could affect MDA activity, the correlation between several manganese species and benzene formation rate is examined, as shown in Figure 3-14. The Mn(2.5)/H-ZSM-5 sample primarily contains isolated Mn^{2+} ion species. It is shown that the MDA activity of the Mn(2.5)/H-ZSM-5 sample is more enhanced than that of the H-ZSM-5 sample, due to the formation of isolated Mn^{2+} ion species. The Mn(5)/H-ZSM-5 sample mainly has isolated Mn^{2+} ion and isolated Mn^{3+} ion species among the manganese species. In comparison with the Mn(2.5)/H-ZSM-5 sample, the Mn^{2+} ion species slightly increases while the isolated

Mn^{3+} ion species greatly increases in the Mn(5)/H-ZSM-5 sample, which exhibits that the MDA activity of the Mn(5)/H-ZSM-5 sample is improved more significantly than that of the Mn(2.5)/H-ZSM-5 sample due to the formation of isolated Mn^{3+} ion species. Consequently, it can be seen that isolated Mn^{2+} ion and isolated Mn^{3+} ion species promote MDA activity and, in particular, isolated Mn^{3+} ion species contributes significantly to the enhancement of the MDA activity. The Mn(7.5) and Mn(10)/H-ZSM-5 samples have isolated Mn^{2+} ion, isolated Mn^{3+} ion, agglomerated MnO, and agglomerated Mn_2O_3 species. It is noted that because the amount of isolated Mn^{2+} ion species is almost constant as the loading amount of Mn exceeds 5wt%, it can be seen that the amount of agglomerated MnO species increases with increasing loading amounts of Mn. Such change of agglomerated MnO species has a similar tendency to that of agglomerated Mn_2O_3 species. Compared to the Mn(5)/H-ZSM-5 sample, the amounts of isolated Mn^{2+} ion and isolated Mn^{3+} ion species are almost the same, while the amounts of agglomerated MnO and Mn_2O_3 species are increased considerably in the Mn(7.5) and Mn(10)/H-ZSM-5 samples. Thus, as the loading of Mn increases, MDA activity decreases gradually due to the formation of agglomerated MnO and Mn_2O_3 species. To sum up, isolated Mn^{2+} ion and isolated Mn^{3+} ion species are the main precursors of active sites, while agglomerated MnO and Mn_2O_3 species is a main inactive site, which diminishes catalytic activity for MDA reaction.

The formation of agglomerated MnO and Mn_2O_3 species on the external zeolite are revealed by the change of BE of Mn 2p and Mn/(Si+Al) ratio with increasing loading amounts of Mn. As shown in Figure 3-4, the BE of Mn 2p decreases as the loading

amount of Mn increases, which is likely related to the dispersion of Mn. If one Mn atom is dispersed in ZSM-5, it will bind to a lot of oxygen because of its unstable nature, which results in higher BE. On the other hand, once agglomerated Mn atom is dispersed in ZSM-5, it will bind to relatively less oxygen, which gives rise to the lower BE. Accordingly, the decrease in the BE of Mn 2p means low dispersion of Mn atom [81]. Furthermore, the actual Mn amount and Mn/(Si+Al) ratio on the surface are compared in the Mn(X)/H-ZSM-5 samples. The increase in the amount of Mn present on the surface is more drastic than the increase in the actual Mn amount. As the amount of Mn increases, this difference increases significantly, and the amount of agglomerated MnO and Mn_2O_3 species increases simultaneously as well. Hence, it is proven that the formation of agglomerated MnO and Mn_2O_3 species on the external of zeolite becomes more abundant as the loading amount of Mn increases.

In order to examine whether the change of isolated Mn^{3+} ion species has a major effect on the activity during MDA reaction, the results of characterization and MDA reaction tests with changing TOS are compared. According to the H_2 TPR results of the pretreated sample and post-reaction sample (50 min), the isolated Mn^{3+} ion and agglomerated Mn_2O_3 species are completely reduced to isolated Mn^{2+} ion and MnO species, respectively, after TOS of 50 min, as exhibited in Figure 3-15.

According to the XPS results, the isolated Mn^{2+} ion and MnO species produced at the beginning of the reaction are not converted to Mn carbide (or oxycarbide) species during the reaction. Combining the results of TPO, UV Raman, and MDA reaction tests shows that the oxidation of isolated Mn^{2+} ion to isolated Mn^{3+} ion species

decreases while benzene yield increases after TOS of 50 min. After a TOS of 130 min, the oxidation of isolated Mn^{2+} ion to isolated Mn^{3+} ion species is markedly reduced while benzene yield has the maximum value. On the other hand, although a LT type coke corresponding to graphite carbon is newly formed, the surface of Mn(5)/ZSM-5 is hardly covered with carbon. It is noted that the oxidation of isolated Mn^{2+} to Mn^{3+} ion species decreases, which underlines that the isolated Mn^{2+} ion species is converted into new manganese species that cannot be oxidized again. Such new manganese species are produced as the reaction proceeds and are significantly formed at a TOS of 130 min in particular, as the benzene yield is the highest, which leads to the conclusion that new manganese species can be considered as an active site for the MDA reaction. Such an activation of manganese species at the beginning of the reaction can be called the induction period of the MDA reaction. To sum up, at the initial stage of the reaction, isolated Mn^{2+} ion species is formed, resulting from the reduction of isolated Mn^{3+} ion species by CH_4, and subsequently isolated Mn^{2+} ion species can be converted to new manganese species that can be a major active site for MDA reaction.

At each TOS of 290 and 850 min, active manganese species slightly increases while LT type coke increases considerably, which results in decreased benzene yield. TPO analysis demonstrates that LT type coke may be ascribed to the carbonaceous deposit species produced on the surfaces of active manganese species. Such carbonaceous deposit species grow larger, which can cover the surface of active manganese species as the reaction proceeds. According to the XRD and BET results, it is observed that pore volume decreases significantly while the crystalline structure of H-ZSM-5 is

well maintained after TOS of 850 min. This means that the formation of excessive carbonaceous deposit species blocks the micro pore of zeolite. Thus, the formation of excessive carbonaceous deposit species on the active manganese species is the primary reason for the deactivation of catalyst due to the blockage of the access of methane to active sites.

Table 3-8. Number of ion exchange step and actual amount of Mn in Mn(IE-X) catalysts made by repeating the ion exchange step with 0.1 M $Mn\cdot(CH_3COO)_2\cdot 4H_2O$ aqueous solution.

Catalyst	Number of ion exchange step	Amount of Mn
Mn(IE-1)/H-ZSM-5	1	1.89wt%
Mn(IE-2)/H-ZSM-5	2	2.30wt%
Mn(IE-3)/H-ZSM-5	3	2.43wt%
Mn(IE-4)/H-ZSM-5	4	2.43wt%

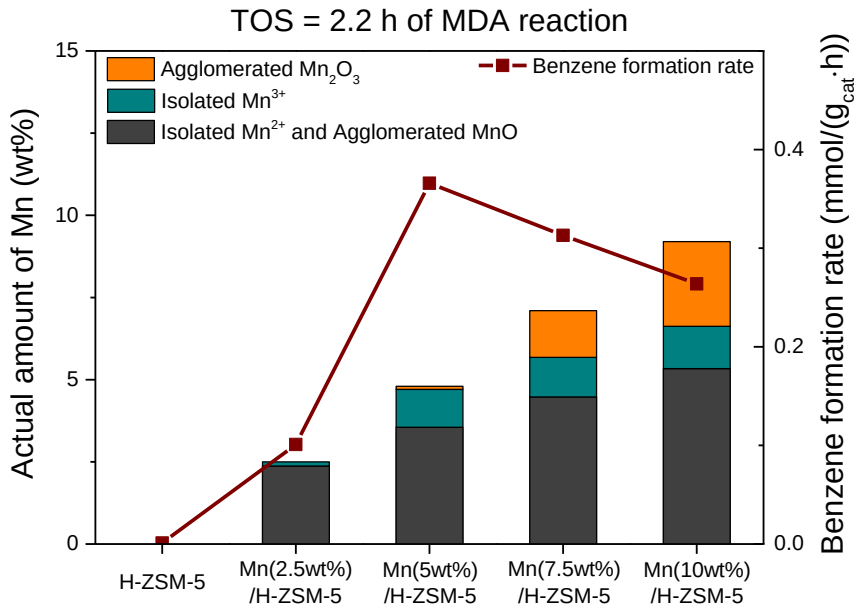

Figure 3-14. Correlation between several manganese species and benzene formation rate.

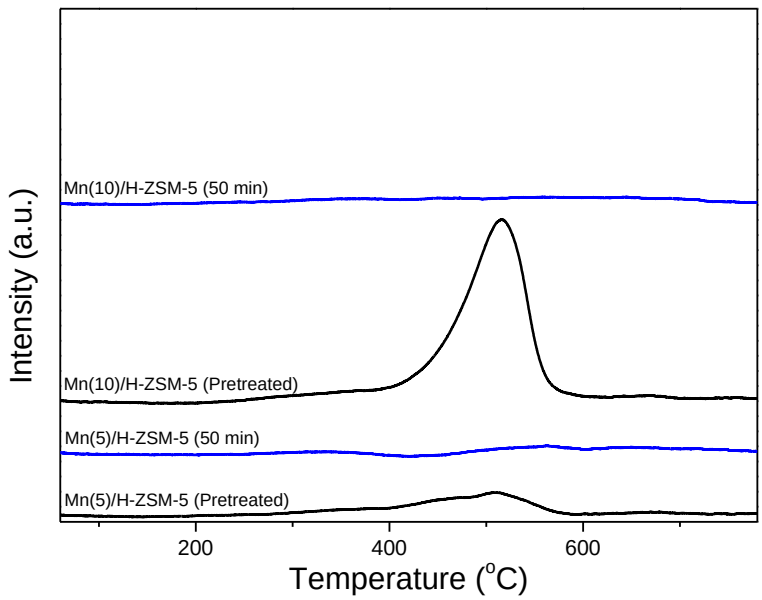

Figure 3-15. H_2 TPR profiles of pretreatment and post-reaction (50 min) in Mn(5) and Mn(10)/H-ZSM-5 samples.

Chapter 4. Summary and Conclusions

In the present work, catalysts using new metal and support were examined in order to enhance activity and ascertain their active site for the MDA reaction. Particularly, catalysts controlling reaction times were investigated to identify deactivation mechanism of the catalysts during the MDA reaction.

In order to investigate the effect of zeolite controlling Si/Al_2 ratio on the performance and deactivation of catalyst for MDA reaction, Mo(5)/H-MCM-22 catalysts with various Si/Al_2 ratios were employed for MDA reaction. We have found that BAS, determined by the Si/Al_2 ratios, stabilizes monomeric Mo oxide species, by promoting to migrate Mo oxides into the micropore of zeolite. In addition, BAS may enhance the distribution of isolated Mo dioxo species anchored to double Al atom. HT type coke is mainly constituted of polyaromatics like naphthalene and anthracene, which is regarded as the primary reason for the deactivation of the catalyst in the MDA reaction since its formation on the micropore openings causes the reduced accessibility of methane inside the micropore of zeolite. Thus, it is found that high dispersion of Mo oxides suppresses the formation of HT type coke and enhances methane conversion rate and benzene formation rate. Furthermore, it is confirmed that the formation of HT type coke is mainly influenced by presence of Mo oxides on the external surface of zeolite rather than BAS, thus eventually leading to conclude that the role of microchannel of zeolite is to primarily supply a shape-selective environment for conversion of methane to benzene. Therefore, it can be suggested that MDA reaction is mostly activated by monofunctional mechanism

employing well dispersed molybdenum carbides in the microchannel of zeolite with shape selectivity as an active site.

To examine the effect of various manganese species on the performance and deactivation of catalyst for MDA reaction, Mn/H-ZSM-5 catalysts with various loading amounts of Mn were applied to MDA reaction. Change of manganese species such as isolated Mn^{2+} ions, isolated Mn^{3+} ion, agglomerated MnO and agglomerated Mn_2O_3 species is investigated as a function of the amount of Mn based on with H_2 TPR, NH_3 TPD and DRIFT analysis. Such characterizations demonstrate that isolated Mn^{2+} ion species is produced by anchoring to BAS and isolated Mn^{3+} ion species is formed from the oxidation of Mn^{2+} ion, anchored to hydroxyl groups (ex-Al-OH and Si-OH), during calcination and pretreatment procedure. Moreover, agglomerated MnO and Mn_2O_3 species are formed by the aggregation and reduction of Mn_2O_3 species on the external surface of zeolite without linkage to any sites, as proven by H_2 TPR and XPS analyses. According to the result of the MDA reaction test, the MDA activity is markedly influenced by manganese species. Among the manganese species, isolated Mn^{2+} ion and isolated Mn^{3+} ion species contribute to the enhancement for the MDA activity, and, in particular, isolated Mn^{3+} ion species greatly improves the MDA activity compared to Mn^{2+} ion species anchored to BAS. This means that isolated Mn^{3+} ion species is a major precursor of active site. By contrast, agglomerated MnO and Mn_2O_3 species reduce catalytic activity by blocking the entrance of the micro pore of zeolite. According to TPR, TPO, and UV Raman analyses, it is verified that the isolated Mn^{3+} ion species is reduced to isolated Mn^{2+} ion species by CH_4, which can be subsequently converted to active manganese

species at the beginning of the reaction. As the reaction proceeds, carbonaceous deposit species is excessively produced on the active manganese species, which is the main reason for the deactivation of catalyst due to the blockage of methane to active sites. To sum up, from the beginning of the MDA reaction, the isolated Mn^{3+} ion species as a main precursor of active site begins to be converted to active manganese species, where it improves MDA activity. As the reaction proceeds, the carbonaceous deposit species is excessively formed on the active manganese species, which gradually diminishes MDA activity.

Bibliography

[1] R. Lin, A.P. Amrute, J. Pérez-Ramírez, Chemical Reviews, 117 (2017) 4182-4247.

[2] J.J. Spivey, G. Hutchings, Chemical Society Reviews, 43 (2014) 792-803.

[3] Monthly Energy Review, U.S. Energy Information Administration, September 2018.

[4] R. Lin, Y. Ding, L. Gong, W. Dong, J. Wang, T. Zhang, Journal of Catalysis, 272 (2010) 65-73.

[5] T.V. Choudhary, S. Banerjee, V.R. Choudhary, Applied Catalysis A: General, 234 (2002) 1-23.

[6] T.H. Lim, S.J. Cho, H.S. Yang, M.H. Engelhard, D.H. Kim, Applied Catalysis A: General, 505 (2015) 62-69.

[7] https://www.bp.com/en/global/corporate/energy-economics/statistical-review-of-world-energy/natural-gas/natural-gas-reserves.html.

[8] S. Ma, X. Guo, L. Zhao, S. Scott, X. Bao, Journal of Energy Chemistry, 22 (2013) 1-20.

[9] S. Majhi, P. Mohanty, H. Wang, K.K. Pant, Journal of Energy Chemistry, 22 (2013) 543-554.

[10] Y. Xu, X. Bao, L. Lin, Journal of Catalysis, 216 (2003) 386-395.

[11] L. Wang, L. Tao, M. Xie, G. Xu, J. Huang, Y. Xu, Catalysis Letters, 21 (1993) 35-41.

[12] J. Gao, Y. Zheng, Y. Tang, J.-M. Jehng, R. Grybos, J. Handzlik, I.E. Wachs, S.G. Podkolzin, ACS Catalysis, 5 (2015) 3078-3092.

[13] V. Abdelsayed, M.W. Smith, D. Shekhawat, Applied Catalysis A: General, 505 (2015) 365-374.

[14] P.L. Tan, C.T. Au, S.Y. Lai, Catalysis Letters, 112 (2006) 239-245.

[15] J.L. Zeng, Z.T. Xiong, H.B. Zhang, G.D. Lin, K.R. Tsai, Catalysis Letters, 53 (1998) 119-124.

[16] L. Wang, R. Ohnishi, M. Ichikawa, Journal of Catalysis, 190 (2000) 276-283.

[17] A. Martínez, E. Peris, Applied Catalysis A: General, 515 (2016) 32-44.

[18] F. Solymosi, J. Cserényi, A. Szöke, T. Bánsági, A. Oszkó, Journal of Catalysis, 165 (1997) 150-161.

[19] D. Ma, Q. Zhu, Z. Wu, D. Zhou, Y. Shu, Q. Xin, Y. Xu, X. Bao, Physical Chemistry Chemical Physics, 7 (2005) 3102-3109.

[20] C. Delitala, M.D. Alba, A.I. Becerro, D. Delpiano, D. Meloni, E. Musu, I. Ferino, Microporous and Mesoporous Materials, 118 (2009) 1-10.

[21] D. Ma, Y. Shu, M. Cheng, Y. Xu, X. Bao, Journal of Catalysis, 194 (2000) 105-114.

[22] Y. Shu, D. Ma, L. Xu, Y. Xu, X. Bao, Catalysis Letters, 70 (2000) 67-73.

[23] N. Kosinov, F.J.A.G. Coumans, E.A. Uslamin, A.S.G. Wijpkema, B. Mezari, E.J.M. Hensen, ACS Catalysis, 7 (2017) 520-529.

[24] B.M. Weckhuysen, D. Wang, M.P. Rosynek, J.H. Lunsford, Angewandte Chemie International Edition in English, 36 (1997) 2374-2376.

[25] P. Mériaudeau, V.T.T. Ha, L.V. Tiep, Catalysis Letters, 64 (2000) 49-51.

[26] L.Y. Chen, L.W. Lin, Z.S. Xu, X.S. Li, T. Zhang, Journal of Catalysis, 157 (1995) 190-200.

[27] Y.H. Kim, R.W. Borry, E. Iglesia, Microporous and Mesoporous Materials, 35 (2000) 495-509.

[28] R.W. Borry, Y.H. Kim, A. Huffsmith, J.A. Reimer, E. Iglesia, The Journal of Physical Chemistry B, 103 (1999) 5787-5796.

[29] H. Liu, W. Shen, X. Bao, Y. Xu, Applied Catalysis A: General, 295 (2005) 79-88.

[30] D. Ma, Y. Shu, X. Han, X. Liu, Y. Xu, X. Bao, The Journal of Physical Chemistry B, 105 (2001) 1786-1793.

[31] J.P. Tessonnier, B. Louis, S. Rigolet, M.J. Ledoux, C. Pham-Huu, Applied Catalysis A: General, 336 (2008) 79-88.

[32] J. Gao, Y. Zheng, J.-M. Jehng, Y. Tang, I.E. Wachs, S.G. Podkolzin, Science, 348 (2015) 686-690.

[33] D. Ma, D. Wang, L. Su, Y. Shu, Y. Xu, X. Bao, Journal of Catalysis, 208 (2002) 260-269.

[34] C.H.L. Tempelman, E.J.M. Hensen, Applied Catalysis B: Environmental, 176 (2015) 731-739.

[35] Y. Song, Y. Xu, Y. Suzuki, H. Nakagome, X. Ma, Z.-G. Zhang, Journal of Catalysis, 330 (2015) 261-272.

[36] W. Ding, G.D. Meitzner, E. Iglesia, Journal of Catalysis, 206 (2002) 14-22.

[37] C.H.L. Tempelman, V.O. de Rodrigues, E.R.H. van Eck, P.C.M.M. Magusin, E.J.M. Hensen, Microporous and Mesoporous Materials, 203 (2015) 259-273.

[38] H. Liu, Y. Li, W. Shen, X. Bao, Y. Xu, Catalysis Today, 93 (2004) 65-73.

[39] X. Dong, Y. Song, W. Lin, Catalysis Communications, 8 (2007) 539-542.

[40] H. Wang, L. Su, J. Zhuang, D. Tan, Y. Xu, X. Bao, The Journal of Physical Chemistry B, 107 (2003) 12964-12972.

[41] L. Liu, D. Ma, H. Chen, H. Zheng, M. Cheng, Y. Xu, X. Bao, Catalysis Letters, 108 (2006) 25-30.

[42] A. Corma, C. Corell, J. Pérez-Pariente, Zeolites, 15 (1995) 2-8.

[43] S. Liu, Q. Dong, R. Ohnishi, M. Ichikawa, Chemical Communications, (1997) 1455-1456.

[44] C.S. Carriço, F.T. Cruz, M.B. Santos, H.O. Pastore, H.M.C. Andrade, A.J.S. Mascarenhas, Microporous and Mesoporous Materials, 181 (2013) 74-82.

[45] C. Li, Journal of Catalysis, 216 (2003) 203-212.

[46] H. Tian, C.A. Roberts, I.E. Wachs, The Journal of Physical Chemistry C, 114 (2010) 14110-14120.

[47] F. Fan, Z. Feng, C. Li, Accounts of Chemical Research, 43 (2010) 378-387.

[48] Y.T. Chua, P.C. Stair, I.E. Wachs, The Journal of Physical Chemistry B, 105 (2001) 8600-8606.

[49] J.P. Tessonnier, B. Louis, S. Walspurger, J. Sommer, M.J. Ledoux, C. Pham-Huu, The Journal of Physical Chemistry B, 110 (2006) 10390-10395.

[50] H. Liu, X. Bao, Y. Xu, Journal of Catalysis, 239 (2006) 441-450.

[51] D.J. Wang, J.H. Lunsford, M.P. Rosynek, Journal of Catalysis, 169 (1997) 347-358.

[52] S. Kikuchi, R. Kojima, H. Ma, J. Bai, M. Ichikawa, Journal of Catalysis, 242 (2006) 349-356.

[53] B.S. Liu, L. Jiang, H. Sun, C.T. Au, Applied Surface Science, 253 (2007) 5092-5100.

[54] C. Li, P.C. Stair, Catalysis Today, 33 (1997) 353-360.

[55] D. Rojo-Gama, M. Signorile, F. Bonino, S. Bordiga, U. Olsbye, K.P. Lillerud, P. Beato, S. Svelle, Journal of Catalysis, 351 (2017) 33-48.

[56] P. Schwach, X. Pan, X. Bao, Chemical Reviews, 117 (2017) 8497-8520.

[57] J.S. Lee, S.T. Oyama, Catalysis Reviews, 30 (1988) 249-280.

[58] L.M. Ioffe, P. Bosch, T. Viveros, H. Sanchez, Y.G. Borodko, Materials Chemistry and Physics, 51 (1997) 269-275.

[59] M. Marczewski, H. Marczewska, React Kinet Catal Lett, 53 (1994) 33-38.

[60] Q. Sun, W.M.H. Sachtler, Applied Catalysis B: Environmental, 42 (2003) 393-401.

[61] A. De Lucas, J.L. Valverde, F. Dorado, A. Romero, I. Asencio, Journal of Molecular Catalysis A: Chemical, 225 (2005) 47-58.

[62] G. Lv, F. Bin, C. Song, K. Wang, J. Song, Fuel, 107 (2013) 217-224.

[63] S. Liu, L. Wang, R. Ohnishi, M. Ichikawa, Journal of Catalysis, 181 (1999) 175-188.

[64] B. Liu, S. Lu, E. Liu, X. Hu, J. Fan, Korean Journal of Chemical Engineering, 35 (2018) 867-874.

[65] L.J. Lobree, I.C. Hwang, J.A. Reimer, A.T. Bell, Journal of Catalysis, 186 (1999) 242-253.

[66] B.M. Lok, B.K. Marcus, C.L. Angell, Zeolites, 6 (1986) 185-194.

[67] J. Carnö, M. Ferrandon, E. Björnbom, S. Järås, Applied Catalysis A: General, 155 (1997) 265-281.

[68] J. Trawczyński, B. Bielak, W. Miśta, Applied Catalysis B: Environmental, 55 (2005) 277-285.

[69] https://xpssimplified.com/elements/manganese.php.

[70] F. Ayari, M. Mhamdi, T. Hammedi, J. Álvarez-Rodríguez, A.R. Guerrero-Ruiz, G. Delahay, A. Ghorbel, Applied Catalysis A: General, 439-440 (2012) 88-100.

[71] Y. Cheng, C. Miao, W. Hua, Y. Yue, Z. Gao, Applied Catalysis A: General, 532 (2017) 111-119.

[72] Z. Sobalík, Z. Tvarůžková, B. Wichterlová, Journal of Physical Chemistry B, 102 (1998) 1077-1085.

[73] P.K. Dutta, M. Puri, The Journal of Physical Chemistry, 91 (1987) 4329-4333.

[74] J. Chen, Z. Feng, P. Ying, C. Li, The Journal of Physical Chemistry B, 108 (2004) 12669-12676.

[75] Y.F. Han, K. Ramesh, L. Chen, E. Widjaja, S. Chilukoti, F. Chen, The Journal of Physical Chemistry C, 111 (2007) 2830-2833.

[76] T.H. Lim, K. Nam, I.K. Song, K.-Y. Lee, D.H. Kim, Applied Catalysis A: General, 552 (2018) 11-20.

[77] D. Ma, Y. Lu, L. Su, Z. Xu, Z. Tian, Y. Xu, L. Lin, X. Bao, The Journal of Physical Chemistry B, 106 (2002) 8524-8530.

[78] P.L. Tan, K.W. Wong, C.T. Au, S.Y. Lai, Applied Catalysis A: General, 253 (2003) 305-316.

[79] W.S. Kijlstra, E.K. Poels, A. Bliek, B.M. Weckhuysen, R.A. Schoonheydt, The Journal of Physical Chemistry B, 101 (1997) 309-316.

[80] F. Kapteijn, A.D. Vanlangeveld, J.A. Moulijn, A. Andreini, M.A. Vuurman, A.M. Turek, J.M. Jehng, I.E. Wachs, Journal of Catalysis, 150 (1994) 94-104.

[81] Y.F. Han, F. Chen, Z. Zhong, K. Ramesh, L. Chen, E. Widjaja, The Journal of Physical Chemistry B, 110 (2006) 24450-24456.

국 문 초 록

천연가스는 청정 에너지 자원으로서 전 세계적에 풍부하게 분포되어 있어 원유를 대신하여 가치 있는 화학 물질을 생산하는 대체 에너지 자원으로 많은 주목을 받고 있다. 그러나 천연가스의 일부가 연소되거나 배출되는데 이는 연간 세계 천연가스 소비량의 약 5%를 차지한다. 천연가스의 주성분은 메탄이며 이는 지구 온난화 잠재력이 이산화탄소의 21 배에 달하는 강력한 온실 가스이다. 따라서 온실 가스 배출을 줄이기 위해 메탄의 효과적인 사용이 필요하다.

메탄은 직접적인 또는 간접적인 방법을 통해 고차 탄화수소로 전환될 수 있다. 두 방법 중에서 메탄 전환에 대한 연구는 주로 간접적인 방법에 적용되어왔다. 그러나 간접적인 방법은 두 단계 공정으로 구성되어 직접적인 방법보다 높은 비용과 많은 시간이 소요된다는 단점을 갖고 있다. 따라서 수십년 동안 메탄을 보다 높은 탄화수소로 전환시키기 위해 경제적인 이점을 지닌 직접적인 방법에 대한 연구가 많이 수행되었다. 다양한 직접적인 방법들 중에서, 메탄 탈수소방향족화 (MDA) 반응은 메탄을 다른 생성물보다 벤젠으로 전환시키는 것이 열역학적으로 유리하기 때문에 상당한 주목을 받고 있다. 비록 MDA 반응이 20 년 이상 연구되어 왔지만, MDA 공정의 상용화를 위하여 촉매 활성을 향상시키고 촉매의 비활성화를 억제하기 위해서는 새로운 금속과 새로운 담체를 이용한 촉매에 대한 연구가 여전히 필요한 실정이다.

제올라이트의 Si/Al_2 비율의 조절이 MDA 반응에서 촉매의 성능 및 촉매의 비활성화에 미치는 영향을 조사하기 위하여, 다양한 Si/Al_2 비율을 갖는 Mo(5)/H-MCM-22 촉매들을 MDA 반응에 적용 하였다. NH_3 TPD, XPS, TPO, UV Raman, STEM-EDS 분석에 따르면, Si/Al_2 비율에 의하여 결정되는 브뢴스테드 산점은 Mo 산화물을 제올라이트의 마이크로 세공으로 이동시키는 것을 용이하게함으로써 Mo 산화물의 단량체를 안정화 시킨다. 이는 활성을 갖는 Mo 산화물 종의 분포에 영향을 미칠 수 있다. 반응 후 촉매들의 TPO 및 UV Raman 분석 결과를 통해, 고온에서 생성되는 코크스는 주로 나프탈렌 및 안트라센과 같은 다환방향족탄화수소 화합물로 구성되며 MDA 반응 동안 촉매의 비활성화를 초래하는 것이 명백히 확인되었다. 고온에서 생성되는 코크스의 형성은 제올라이트 외부 표면에 존재하는 Mo 산화물의 양에 의해 주로 영향을 받으며, 이는 제올라이트의 마이크로 세공의 주요 역할이 MDA 반응시 형상 선택적인 환경을 제공하여 메탄을 주로 벤젠으로 전환시키는 것을 나타낸다. 요약하면, 브뢴스테드 산점의 증가는 Mo 산화물의 분산을 증가시키며, 이는 고온에서 생성되는 코크스의 형성을 억제하면서 동시에 메탄 전환율 및 벤젠 형성 속도를 향상시킨다.

다양한 Mn 종들이 MDA 반응에서 촉매의 성능과 촉매의 비활성화에 미치는 영향을 알아보기 위해, 다양한 Mn 의 담지량을 갖는 Mn/H-ZSM-5 촉매들을 MDA 반응에 적용 하였다. H_2 TPR, NH_3 TPD,

DRIFT 분석에 따르면 고립된 Mn^{2+} 이온, 고립된 Mn^{3+} 이온, 응집된 MnO, 응집된 Mn_2O_3 종과 같은 다양한 망간 종들의 존재는 Mn 의 담지량에 따라 변화된다.

Mn 종들 중에서, Mn 의 담지량이 5wt% 이하일 때, 고립된 Mn^{2+} 이온과 고립된 Mn^{3+} 이온 종은 주로 Mn^{2+} 이온과 브뢴스테드 산점 및 제올라이트의 수산기(ex-Al-OH 및 Si-OH)의 결합에 의해 각각 생성되는 것을 증명하였다. 이에 반해서, Mn 의 담지량이 5wt% 이상일 때, 응집된 MnO 와 Mn_2O_3 종은 H_2 TPR 및 XPS 분석에 의해 입증된 바와 같이 임의의 부위에 정착하지 않고 제올라이트의 외부 표면 상에 존재한다. 이러한 Mn 종들 중에서, 고립된 Mn^{3+} 이온 종은 MDA 반응에 대한 활성 사이트의 전구체로서 필수적인 역할을 한다. 한편, 응집된 MnO 와 Mn_2O_3 종은 제올라이트의 마이크로 세공의 입구를 막음으로써 촉매 활성을 감소시킨다. H_2 TPR, TPO, UV Raman 분석을 종합하면, 고립된 Mn^{2+} 이온 종은 고립된 Mn^{3+} 이온 종의 메탄에 의한 환원으로부터 생성되고, 이어서 다시 산화 될 수 없는 새로운 망간 종으로 전환됨을 입증한다. 반응이 진행됨에 따라 코크스는 활성 망간 종에 과도하게 형성되어 메탄의 활성 사이트로의 접근을 막아서 촉매의 비활성화를 야기한다. 요약하면, MDA 반응의 초기 단계에서 고립된 Mn^{3+} 이온 종으로부터 생성되는 새로운 망간 종이 주요한 활성 사이트이며 반면, 활성을 갖는 망간 종에 과도한 코크스 형성이 촉매의 비활성화에 대한 주된 이유이다.

주요어: 메탄 탈수소방향족화 반응; Mo/H−MCM−22; 촉매의 비활성화; Si/Al_2 비율; 브뢴스테드 산점; Mn/H−ZSM−5; 망간 종

학번: 2015−30217